Published November 22, 2019

Original Research

Core Ideas

- 4-yr monitoring of soil water content dynamics for different plant types.
- Horizontal crosshole GPR at the field-plot scale sampled ~65 m^3.
- Natural, irrigated, and sheltered treatments in gravelly and clayey–silty soils.
- Consistent patches of soil water content were observed along horizontal slices using GPR.
- Results enable improved investigation of soil–plant–atmosphere interactions.

Monitoring Soil Water Content Using Time-Lapse Horizontal Borehole GPR Data at the Field-Plot Scale

Anja Klotzsche,* Lena Lärm, Jan Vanderborght, Gaochao Cai, Shehan Morandage, Miriam Zörner, Harry Vereecken, and Jan van der Kruk

Ground penetrating radar (GPR) has shown a high potential to derive soil water content (SWC) at different scales. In this study, we combined multiple horizontal GPR measurements at different depths to investigate the spatial and temporal variability of the SWC under cropped plots. The SWC data were analyzed for four growing seasons between 2014 and 2017, two soil types (gravelly and clayey–silty), two crops (wheat [*Triticum aestivum* L.] and maize [*Zea mays* L.]), and three different water treatments. We acquired more than 150 time-lapse GPR datasets along 6-m-long horizontal crossholes at six depths. The GPR SWC distributions are distinct both horizontally and vertically for both soil types. A clear change in SWC can be observed at both sites between the surface layer (>0.3 m) and subsoil. Alternating patches of higher and lower SWC, probably caused by the soil heterogeneity, were observed along the horizontal SWC profiles. To investigate the changes in SWC with time, GPR and time-domain reflectometry (TDR) data were averaged for each depth and compared with changes in precipitation, treatment, and soil type. The high-temporal-resolution TDR and the large-sampling-volume GPR show similar trends in SWC for both sites, but because of the different sensing volumes, different responses were obtained due to the spatial heterogeneity. A difference in spatial variation of the crosshole GPR SWC data was detected between maize and wheat. The results for this 4-yr period indicate the potential of this novel experimental setup to monitor spatial and temporal SWC changes that can be used to study soil–plant–atmosphere interactions.

Abbreviations: EM, electromagnetic; EMI, electromagnetic induction; ERT, electrical resistivity tomography; GPR, ground penetrating radar; SV, sampling volume; SWC, soil water content; TDR, time domain reflectometry; ZOP, zero-offset-profile.

A. Klotzsche, J. Vanderborght, S. Morandage, M. Zörner, H. Vereecken, and J. van der Kruk, Agrosphere (IBG-3), Institute of Bio- and Geosciences, Forschungszentrum Jülich, 52428 Jülich, Germany; L. Lärm and G. Cai, formerly Agrosphere (IBG-3), Institute of Bio- and Geosciences, Forschungszentrum Jülich, 52428 Jülich, Germany; G. Cai, currently at Dep. of Soil Physics, Bayreuth Center of Ecology and Environmental Research (BayCEER), Univ. of Bayreuth, 95447 Bayreuth, Germany. *Corresponding author (a.klotzsche@fz-juelich.de).

Received 1 May 2019.
Accepted 12 Oct. 2019.
Supplemental material online.

Citation: Klotzsche, A., L. Lärm, J. Vanderborght, G. Cai, S. Morandage, M. Zörner, H. Vereecken, and J. van der Kruk. 2019. Monitoring soil water content using time-lapse horizontal borehole GPR data at the field-plot scale. Vadose Zone J. 18:190044. doi:10.2136/vzj2019.05.0044

Soil water content (SWC) is an important state variable that is linked to several important soil functions and strongly depends on the internal organization of the soil–plant system. Soil water is important for crop growth and food and feed production, can percolate to deeper layers and replenish aquifers, can carry solutes toward the groundwater, and is required by microorganisms that regulate biogeochemical cycles. Soil water and related soil processes vary considerably in space and time due to spatially variable soil properties and highly dynamic boundary conditions (e.g., precipitation, evapotranspiration). Understanding and subsequently predicting soil processes require information on SWC and how it varies in time and space. Soil water content can be monitored using in situ sensors (that can be connected to the internet and provide seamless data streams of local SWC) and using remote sensing from satellites (e.g., Simmer et al., 2015; Vereecken et al., 2016). In situ sensors have a small spatial support so that a large number of sensors would be required to obtain an accurate and precise estimate at large scales. Another challenge is to infer connected patterns of SWC that represent preferential flow paths in the soil or landscape with in situ sensors since they do not provide a dense spatial coverage. The limitation of satellite SWC products is that they have a low spatial resolution and most sensors are sensitive to the SWC in only the upper few centimeters of the soil profile. To fill the gap between in situ sensors and satellite products, high-resolution nondestructive geophysical imaging

methods show an increasing potential to further improve the detection, monitoring, and imaging of in situ soil properties at the field scale. Near-surface geophysical methods, such as electrical resistivity tomography (ERT), electromagnetic induction (EMI), and ground-penetrating radar (GPR) provide maps of the SWC at the field-plot scale up to the field and catchment scales with dense spatial coverage and can be used to enhance agricultural, environmental, and land surface models (e.g., Binley et al., 2015). Several geophysical studies have been performed to investigate the soil–plant system using time-lapse monitoring data at the laboratory or field scale, applying mainly ERT, time domain reflectometry (TDR), or EMI tools. For example, root water uptake was investigated with time-lapse ERT within lysimeters and for different cropping systems in the field (Garré et al., 2011, 2013). Several other field studies were performed using a fixed, installed ERT monitoring transect to study the soil–plant interaction of orange [*Citrus* × *sinensis* (L.) Osbeck] trees (e.g., Vanella et al., 2018) and crops like wheat (*Triticum aestivum* L.) (e.g., Shanahan et al., 2015) and maize (*Zea mays* L.) (e.g., Michot et al., 2003; Beff et al., 2013). Even though all these studies successfully demonstrated the potential to derive soil water and plant interactions, each of the methods has limitations. For example, TDR provides point information, ERT and EMI are sensitive to several other factors beyond water content, and EMI provides good coverage in space but with limited spatial resolution.

The advantage of GPR compared with ERT and EMI is that GPR provides information about the relative dielectric permittivity ε_r of the soil, which is more directly related to SWC than the electrical conductivity σ (Huisman et al., 2003; Klotzsche et al., 2018). Since the emergence of the field of hydrogeophysics (Binley et al., 2015), GPR has shown a high potential to map, detect, and monitor SWC changes to improve the hydrological characterization of the vadose zone with the highest possible resolution compared with other geophysical methods because of the use of high frequencies between 25 MHz and 1.6 GHz (e.g., Binley et al., 2002; Linde et al., 2006; Dafflon et al., 2011; Paz et al., 2017; Steelman et al., 2017). Because of the large difference between the relative dielectric permittivity of air, $\varepsilon_r = 1$, and water, $\varepsilon_r = 80$, it can be used to obtain the SWC in the vadose zone. To investigate flow and transport processes, time-lapse GPR measurements with a high spatial and temporal resolution can be linked to soil hydrological parameters such as hydraulic conductivity. For example, Looms et al. (2008b) investigated unsaturated flow and transport processes using crosshole GPR and ERT in alluvial sandy sediments and estimated hydraulic patterns (Looms et al., 2008a). Strobach et al. (2014) combined surface and borehole GPR measurements to monitor rainfall infiltration in the vadose zone and to investigate characteristic infiltration regimes.

Allroggen et al. (2015) measured and monitored flow processes in the near subsurface using three-dimensional surface GPR measurements during rainfall experiments and associated patterns of travel-time changes in GPR signals with SWC variations. To further extend our knowledge about the relations between GPR data and hydrological parameters, controlled environments are essential. At the laboratory scale, GPR measurements can be performed in lysimeters (e.g., Schmalholz et al., 2004; Wijewardana et al., 2017). Klenk et al. (2015) and Jaumann and Roth (2018) used surface GPR data to study SWC changes during pumping and infiltration experiments at the ASSESS site of the University of Heidelberg: a 20-m-long, 4-m-wide, and approximately 1.9-m-deep tank in which a known heterogeneous structure of different sand layers was created. Due to the control of these layers on the spatiotemporal distribution of SWC, which could be observed with surface GPR, they could infer the hydraulic properties of the layers. Furthermore, several surface GPR studies have been performed to detect and characterize soil–plant systems and the influence of the SWC on plant development. For example, Rodríguez-Robles et al. (2017) used GPR to map tree roots. Wijewardana and Galagedara (2010) investigated the spatial and temporal variability of the SWC for different crop types. Nevertheless, the characterization of the climate–plant–soil interaction at the plot scale has been very limited until now, and long-term monitoring using GPR or other geophysical methods during serval growing seasons are very sparse in the literature (e.g., Jayawickreme et al. [2010] for a 2-yr ERT study). The disadvantages of "classical" GPR is that it cannot be used in an automated monitoring mode and that the interpretation of surface GPR measurements to derive depth profiles of SWC is not straightforward in the absence of clear reflections and/or gradients. Cross-borehole GPR can be used to investigate the deeper near-subsurface between boreholes. Borehole GPR measurements can provide higher resolution insights into the subsurface and are well suited to characterize the vadose zone (e.g., Binley et al., 2002; Klotzsche et al., 2013) and to monitor infiltration and recharge processes (e.g., Looms et al., 2008a). Horizontal cross-borehole acquisitions provide a direct link of SWC variations between the tubes at certain depth slices and are well suited to investigate how SWC varies in both time and space at a certain depth due to infiltration, redistribution, and plant water uptake at the plot scale. Parkin et al. (2000) first applied crosshole GPR measurements in horizontal tubes below a wastewater trench at the 1.2-m depth. They applied zero-offset profiling (ZOP) that provided an average SWC along the tubes and multi-offset gathers to estimate a two-dimensional SWC distribution in a horizontal plane. Redman et al. (2000) and Galagedara et al. (2002) used GPR in horizontal boreholes to study the temporal and spatial variation of SWC under wetting and drying conditions. These studies indicated the potential to detect and map zones of higher water content in between tubes that could be linked to preferential flow paths at the plot scale, which are difficult to obtain using other methods. All these studies mainly concentrated on water content changes without considering the effect of plants and atmospheric conditions. Especially the impact of plants has not been investigated so far using horizontal borehole GPR data. The challenging aspect is that GPR is able to retrieve SWC for a certain domain, but without further information it is very difficult to distinguish between the part of the water in the soil and water related to roots. For tree roots, al Hagrey (2007) stated a variation of the permittivity

between 4.5 for dry wood up to 22 for wet wood, which is a similar range as, for example, dry and wet sand. Therefore, to differentiate between soil and finer root effects on the permittivity and SWC, long-term monitoring that captures different variations of both are necessary.

In this study, we used long-term time-lapse horizontal borehole GPR data to monitor and characterize the SWC variation caused by plants for different surface treatments in two different soil types. The main aim of this study was to investigate how the SWC can be observed at high temporal and spatial resolution. Since boreholes were installed at different depths, we also tested whether the vertical variations in SWC could be detected with GPR. A special focus was to improve the understanding of how small-scale soil changes affect plant growth at the plot scale (e.g., zones of preferential flow) and how the SWC changes during several measurement seasons for different soil and plant types. As part of it, we characterized the field-plot-scale soil heterogeneity by capturing the structural organization of the soil (layering and texture) using GPR. Therefore, we compared GPR-derived water contents with TDR measurements, and we performed full waveform simulations to evaluate the effect of the sharp contrast of dielectric permittivity at the soil surface and the effect of vertical variations in SWC on the GPR-derived vertical water content profiles. By monitoring the SWC and its variation in a field plot during four growing seasons, we investigated the persistency of the patterns and the magnitude of the spatial SWC variations and distinguished a temporally stable component from a variable component that is linked to either temporally varying soil properties or changing rooting patterns between different growing seasons or crops.

Experimental Setup

Test Site and Instrumentation of the Minirhizotrons

Two minirhizotron facilities were installed in 2012 and 2014 at the Selhausen site, Germany, which is part of the TERENO-Rur Hydrological Observatory (e.g., Weihermüller et al., 2007; Bogena et al., 2018). The field is located at a transition zone between the upper and lower terraces of the Rhine–Meuse river system (see Fig. 1), which corresponds with a transition between a soil with a high gravel content and low apparent electrical conductivity in the upper part of the field and a soil with a clayey and silty texture and a higher electrical conductivity in the lower part of the field (Rudolph et al., 2015). To cover this variation in soil properties, one minirhizotron facility was installed in the upper part, R_{UT}, and the other one in the lower terrace, R_{LT}. The so-called minirhizotron is an installation that allows repeatable and non-invasive measuring of plant roots and studying root growth in interaction with changing soil conditions (Cai et al., 2016). During the past years, several geophysical and hydrological studies have been performed at Selhausen test site (e.g., Huisman et al., 2003; Busch et al., 2014; von Hebel et al., 2014; Rudolph et al., 2015). A weather station is installed by the TERENO project providing,

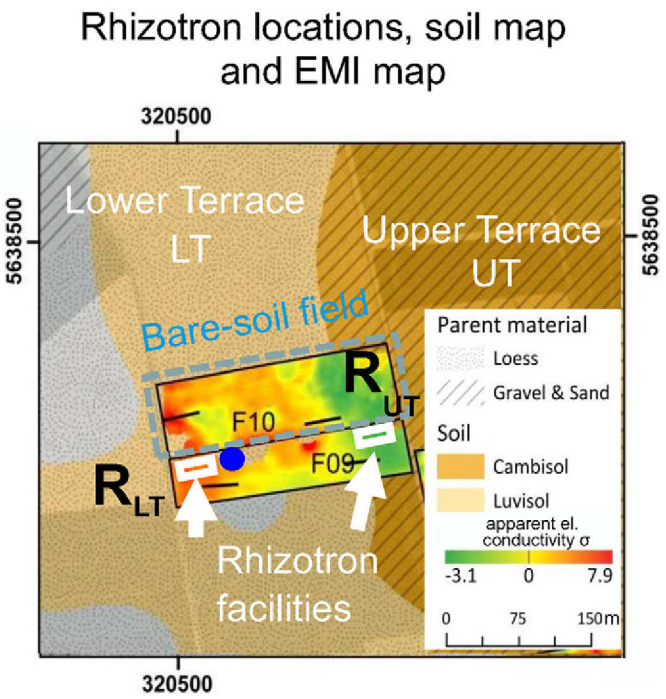

Fig. 1. Location of the minirhizotron facilities indicated on the electromagnetic induction (EMI) and soil map of the Selhausen test site. One rhizotron is located in the upper terrace (R_{UT}) and one in the lower terrace (R_{LT}) of the bare-soil field of the test site, and both are indicated with boxes. The R_{UT} and R_{LT} are positioned in lower and higher apparent conductivity areas, respectively, illustrating the different soil properties of the terraces. The blue dot indicates the location of the weather station. The map is modified from Rudolph et al. (2015).

e.g., precipitation and temperature values (blue dots in Fig. 1). The groundwater table depth is located between 3 and 5 m below the surface, depending on seasonal fluctuations.

Both facilities are equipped to obtain full access to the near-surface soil volume of 1.2-m depth by 9-m width by 6-m length. For monitoring purposes, horizontal tubes with a total length of 7 m were installed at six different depths between 0.1 and 1.2 m, with three replicates for three treatments in both facilities (Fig. 2a and 2c). The boreholes were separated by 0.75 m. To avoid interferences between the different tubes, the boreholes are shifted horizontally (see Fig. 2c). In each facility, three 3- by 7-m plots received different water treatments: rainfed (natural conditions), irrigated, and sheltered. The facilities provided the opportunity to study the spatiotemporal variations of SWC under these three different treatments at each site (Fig. 2b). The R_{UT} site was excavated in layers and, after the boreholes where installed, refilled trying to keep the former layering and compaction of the soil. At R_{LT}, a horizontal drilling device was used to install the boreholes, hence the soil is almost undisturbed. The tubes were drilled with a special tool designed by the Engineering und Technologie department (ZEA-1) of the Forschungszentrum Jülich GmbH. A sensor network with TDR sensors and one tensiometer was installed at each borehole depth and each treatment plot. For each treatment plot, four TDRs per depth were installed that measure the SWC hourly (for more details, see Cai et al., 2016). The TDR sensors are

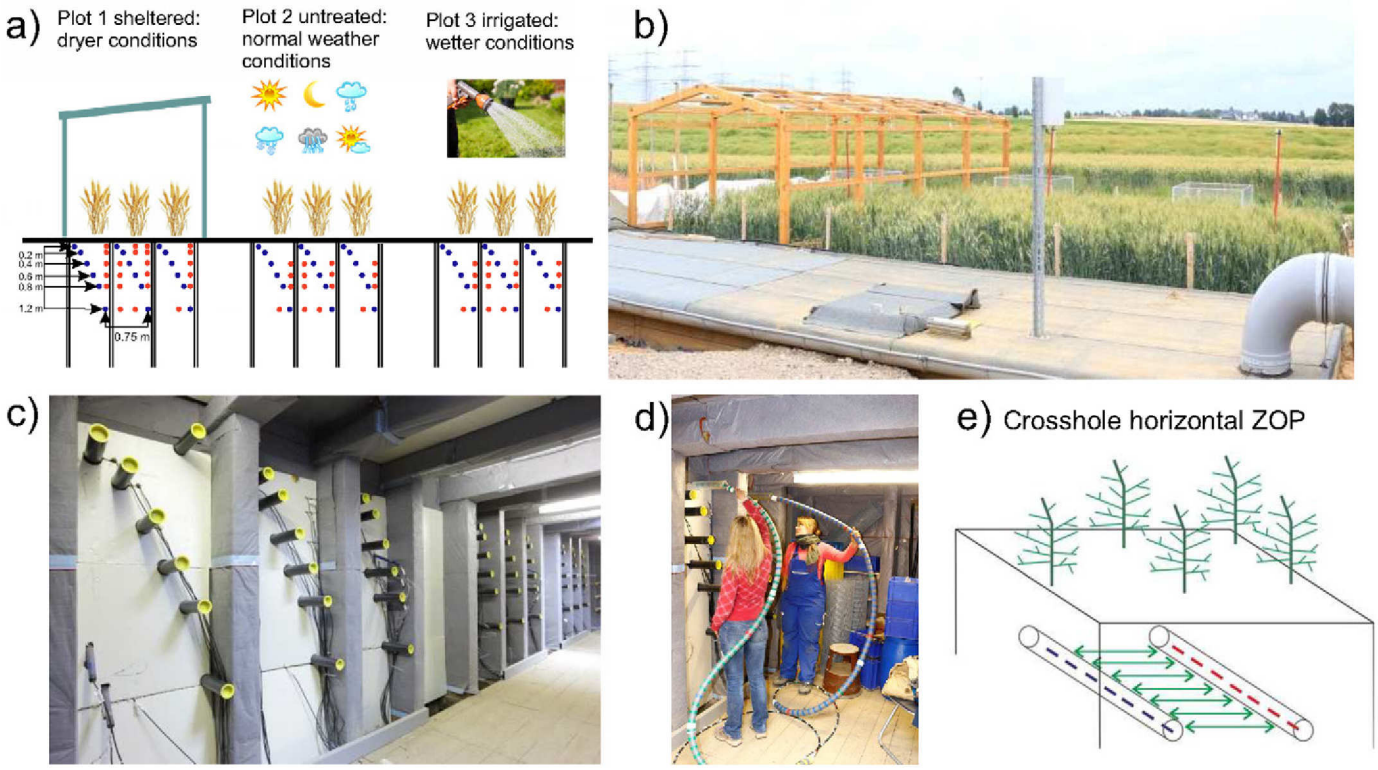

Fig. 2. (a) Schematic setup of the minirhizotron facility at the Selhausen test site, Germany, with the location of the horizontal boreholes and the time domain reflectometry (TDR) sensors indicated with blue and red dots; (b) picture of the facility from the top during the growing season; (c) picture of the facility inside; and (d) when measurements are performed; and (e) schematic setup of the zero-offset profile (ZOP) measurements along tubes at the same depth to obtain depth slices.

a three-rod system with a rod length of 200 mm and a rod separation of 26 mm. All TDRs are located 0.75 m away from the facility wall. Note that stones and gravel larger than 60 mm were removed around the places where the TDR sensors were installed (red dots in Fig. 2a). Due to compaction and erosion of the soil, the original planned depth of the tubes of 0.1 to 1.2 m was slightly lowered by 4 cm (manually checked different times per year).

In this study, we concentrated on the growing seasons of 2014, 2015, and 2016, when winter wheat (cv. Ambello) and summer wheat (cv. Scirocco) was sown at both facilities. Subsequently, we collected data for 2017, when maize (cv. Zoey) was sown. The wheat was planted in narrow rows with a separation of 12 cm, and the maximum crop height was approximately 0.95 m. The maximum observed rooting depth for the winter wheat was the same at all three plots at 0.8 and 1.2 m for R_{UT} and R_{LT}, respectively (Cai et al., 2016). The maize was planted with a row separation of 0.75 m and at the end of the measurement period the plants reached a maximum height of approximately 2.1 m, and a maximum rooting depth of around 0.8 and 1.5 m was observed for R_{UT} and R_{LT}, respectively. The maize plants showed a gradation in height for the different plots (higher in the irrigated plot). Note that after 2016 no shelter was installed anymore because of the height of the plants. Instead, two

Table 1. Measurement days for the upper terrace (R_{UT}) and lower terrace (R_{LT}) rhizotrons. Note that for each day, a minimum of one zero-offset profile was measured across the entire distance per depth.

Year	R_{UT}	R_{LT}	Crop	Sowing	Emergence	Flowering	Harvest
	——— d ———						
2012	23	–	–	–	–	–	–
2013	7†	–	winter wheat	nk‡	nk	nk	nk
2014	19	15	winter wheat	30 Oct. 2013	nk	21 May 2014	17 July 2014
2015	17	16	summer wheat	17 Mar. 2015	21 Mar. 2015	8 June 2015	30 July 2015
2016	22	21	winter wheat	26 Oct. 2015	1 Nov. 2015	3 June 2016	26 July 2016
2017	22	22	maize	5 May 2017	9 May 2017	14 July 2017	16 Sept. 2017

† In October 2013, an infiltration experiment was additionally performed at R_{UT} at the sheltered plot, resulting in two extra undisturbed measurement days. Normally both facilities were measured on the same day.
‡ nk, not exactly known for this event.

rainfed plots were used. Table 1 indicates the crop and the sowing, emergence, flowering, and harvest times. After harvest, bare soil conditions were present in the three plots.

GPR Crosshole Measurements and Acquisition of Time Series

To map SWC at several depths and positions on a weekly basis, we used the ZOP technique. In this technique, the transmitter is positioned in one borehole, while the receiver is located in another borehole, and both antennae are moved simultaneously to the next position with a constant spacing between the measurement points (Fig. 2e). The ZOP measurements were performed using 200-MHz PulseEKKO borehole antennae (Sensors & Software) (Fig. 2d; Table 1) with a horizontal resolution of 5 cm. Because of the known distance between the transmitter and receiver, a velocity profile along the boreholes can be calculated assuming that the rays travel straight between the antennae (e.g., Binley et al., 2002; Looms et al., 2008b). The ZOPs were measured in horizontal depth slices with a spatial separation of 5 cm and a borehole separation of 0.75 m at all depths and three lateral positions representing the different treatments of the plots. This resulted in a dataset for each measurement day covering a soil volume of about 1.2-m depth by 9-m width by 6-m length. In total, around 300 single traces per depth layer were recorded. Since 2016, additional geophysical measurements such as electrical impedance tomography have been performed at R_{LT}. To avoid interferences between the two techniques, 2 m of the GPR measurements were removed and not further analyzed.

GPR Data Analysis

To retrieve quantitative soil properties from the GPR ZOP data, several preprocessing steps are necessary. First, we applied a de-wow filter to reduce low-frequency noise in the measured GPR data. Second, a time-zero correction of the data was applied, which is necessary to account for time shifts of the data during the measuring period that can be caused by thermal drift, electronic instability, cable length differences, and variations in antennae coupling. A common method for the time-zero estimation is to record repeated wide-angle reflection and refraction (WARR) measurements in the air using the borehole antennae to determine an absolute time zero and estimate individual time zeros for each ZOP by time interpolation, whereby the transmitter antenna is fixed at a certain location while the receiver antenna is moved stepwise along a profile with a fixed spacing of 0.1 m. Normally, at least three WARRs per facility were measured per day. One example of this procedure is shown in Fig. 3, where four WARRs were measured during the measurement period. For each of these WARRs the first arrival air wave was picked and the actual time zero was estimated using the known air velocity. In this case, the time zero was around 17 ns, and a variation of the time zero of approximately 0.35 ns during the measurement period can be noticed. The time-zero estimates of the different WARRs were linearly interpolated, and the ZOP measurements in between were corrected using the corresponding time zero as shown by the blue dots. For example, for dry (ε_r = 9) or wet (ε_r = 24) conditions in the rhizotrons, the influence of a time shift of 0.35 ns can result in a difference of up to 1.8 or 2.2% in SWC, respectively. Therefore, to avoid these errors, detailed and accurate time-zero calibrations are essential.

After the GPR data are time-zero corrected, the first breaks of the ZOP data are picked using an automated, user-controlled picking routine. This routine was used due to the huge amount of data available and to avoid inconsistencies in the picking by different users to ensure constant and precise estimation of the first break. The automatic picking routine is able to find the maximum of the traces but not the actual needed first break. Therefore, in the first step, we defined the time shift between the automatically found overall maximum of the traces and the actual first break point. This was done for the different measurement type (WARR and ZOP) data separately and by hand picking several noise-free traces of the entire dataset per test site and day. These two types of time shifts between the first break and the first maximum were estimated for each measurement day and facility separately, and it was assumed that these shifts did not change during the measurement time of one facility. Note that for all the data analyses presented here, the same person defined these constants to avoid user influences. In a second step, the automatic picking routine determined the overall maximum of all traces and subtracted the predefined constant time shift from the automatically picked maximum.

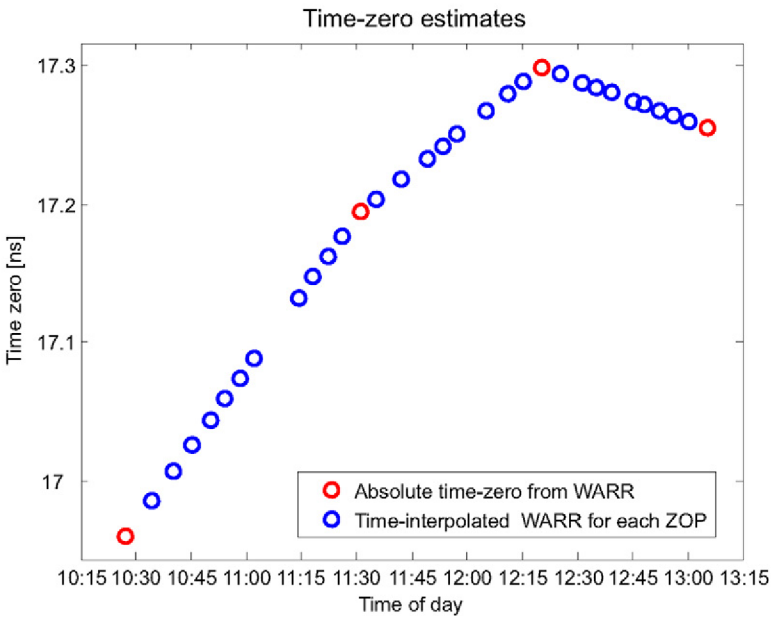

Fig. 3. Example for the time-zero (t_0) estimation obtained from the wide angle reflection and refraction (WARR) measurements (red) during the measurement period of one facility and the interpolated t_0 for all the measured zero-offset profiles (ZOPs, blue).

Using the known distance between the boreholes (0.75 m) and the first breaks of the ZOP, the electromagnetic (EM) wave velocity within the medium is calculated, which can be converted into relative permittivity ε_r of the soil using

$$\varepsilon_r = \left(\frac{c}{v}\right)^2 \quad [1]$$

where v is the EM velocity and c is the speed of light. Both WARR analysis for determining the absolute time zero and ZOP analysis to obtain GPR travel times depend on an accurate and precise picking of the first arrival signals; otherwise errors can occur in the permittivity estimates. Normally for GPR applications, far-field conditions are assumed, where no interferences with the antennae are expected, meaning that the antennae separations should be at least two times larger than the wavelength. In the near-field regime (below one wavelength), the propagation of EM waves is interfered with by the antennae. Depending on the soil properties, the far-field conditions were not always reached for the borehole separation of 0.75 m and the frequencies of the 200 MHz antennae, which are the highest of commercially available borehole antennae. This is particularly important for R_{UT}, where a longer wavelength than at R_{LT} can be expected. This should be considered in the data analysis and picking of the first arrivals. For example, the first break picking in very dry soil is very difficult because no clear first break point is present in the data (long and slow rise of the trace). For such days, the time shift for the ZOP data was defined using only data where a clear point could be chosen (normally deeper depths that were wetter) and was then applied to all data of this day.

First tests indicated that the permittivities of the uppermost depth slice at the 0.1-m depth were usually underestimated compared with GPR data for the 0.2-m depth and showed significantly lower and unrealistic values compared with the permittivities of the underlying depth slices. Because of the small distance between the air–soil interface and the shallow boreholes, an interference of the critically refracted air wave and direct wave is present (more details in Klotzsche et al., 2016). Therefore, we investigated the influence of the air and direct wave interaction on the GPR traces and the retrieved permittivities and water contents using full-waveform simulations (see Appendix A). Summarizing the synthetic studies of Appendix A, using standard travel-time picking procedures, the travel time of the EM wave through the soil is underestimated for the shallow boreholes at 0.1-m depth and no reliable SWC can be obtained. Therefore, these data are not shown in the following. Note that for the depth of 0.2 m also a minor effect can be expected, especially under dry soil conditions.

Furthermore, we investigated the influence of the GPR picked permittivity if gradients or discontinuities in permittivity depth profiles at layer interfaces are present in the subsurface (see Appendix B). The standard first-break picking approach of the travel times assumes that the waves travel directly and on a straight line between the transmitter and receiver antennae. Appendix B illustrates using a second synthetic study how strong and abrupt changes in water contents across layer interfaces or across infiltration or drying fronts influence ray-based estimates of SWC. In particular special attention needs to be drawn toward the interpretation of the topsoil SWC, for instance when a wetted soil is overlying drier subsoil. Such a condition could occur during an infiltration event.

Soil Water Content Derived from GPR and TDR Data

To convert the relative permittivity to SWC, appropriate empirical or petrophysical models are necessary (Huisman et al., 2003; Steelman and Endres, 2011). In general, these relationships can be divided into empirical models, volumetric mixing formulas, and effective medium approximations. Empirical relationships like Topp's equation (Topp et al., 1980) require very limited information about the soil type. In contrast, volumetric mixing formulae relate the measured bulk permittivity to the individual components within the system, weighted by their volume fractions. Effective medium approximations extend this mixing approach by considering structural and textural contributions to formulate microscale geometric models instead of a function of only porosity ϕ and water content θ. For the right choice of the most appropriate model, information about the soil is needed. For this study, we used the Complex Refractive Index Model (CRIM) with a geometry factor of 0.5 considering a three-phase system using air, water, and soil components under consideration of the soil porosity ϕ (Roth et al., 1990; Steelman and Endres, 2011):

$$\mathrm{SWC} = \frac{\sqrt{\varepsilon_r} - (1-\phi)\sqrt{\varepsilon_s} - \phi}{\sqrt{\varepsilon_w} - 1} \quad [2]$$

where ε_r is the relative bulk permittivity, ϕ is the soil porosity, and ε_w and ε_s are the relative dielectric permittivity of water and soil particles, respectively. For both facilities, R_{UT} and R_{LT}, higher porosities of 0.33 and 0.4 were considered for the topsoil layer (0–0.3 m) and 0.25 and 0.35 for the subsoil, respectively (Weihermüller et al., 2007). The permittivity of water at 10°C is $\varepsilon_w = 84$, and the permittivity of the soil ε_s was considered to be 4.7 and 4.0 for R_{UT} and R_{LT}, respectively (Robinson et al., 2005). For R_{LT}, the relations obtained by CRIM were very similar to the empirical Topp equation (Topp et al., 1980), which was used by Cai et al. (2016) to derive SWC from TDR measured ε_r. For the stony soil at R_{UT}, CRIM deviated from Topp's equation, and Cai et al. (2016) used CRIM to derive the SWC from TDR-measured permittivity.

Comparison of GPR and TDR Soil Water Contents

The TDR sensors have a high temporal resolution but a limited spatial coverage compared with the GPR measurements. Several other studies have indicated a good correlation between SWC derived by TDR and surface GPR using the direct groundwave velocity for different soil state conditions (e.g., Huisman et al., 2002). To better quantify the sensing volume of the horizontal

crosshole GPR, we performed a detailed analysis similar to that of Galagedara et al. (2002) by investigating the sampling volume for the different soils and states. The sampling zone for borehole GPR is often defined by the Fresnel zone as a three-dimensional volume (Fresnel volume) and is dependent on the distance between the antennae, center frequency, and permittivity of the medium. The Fresnel volume is described by an ellipsoid with its focus points at the location of the antennae positions. Therefore, the Fresnel zone is considered an elliptical region perpendicular to the ray paths in the center of the ellipsoid. We calculated the sampling volume SV and the radius of the Fresnel zone of both facilities for minimum, intermediate, and maximum observed permittivity and SWC (Table 2). Because of the general lower permittivity values for R_{UT}, the radius of the Fresnel zone R_{FR} and SV are larger than those of R_{LT}. The radius of the Fresnel zone for average permittivity is 0.39 and 0.32 m for R_{UT} and R_{LT}, respectively. For very dry conditions, this radius can reach almost 0.5 m for R_{UT}. Note that these calculations do not consider inhomogeneity caused by infiltration events, rapid drainage, or medium properties changes. The SV for R_{UT} and R_{LT} ranges from 0.26 to 0.53 and 0.17 to 0.3 m^3, respectively. In contrast, the SV of a TDR sensor is approximately 0.005 m^3 and much smaller (at least 30 times) than for GPR (e.g., Ferré et al., 1998; Hinnel et al., 2006). To compare GPR SWC with the TDR SWC values between 2014 and 2016, we averaged the horizontal GPR SWC values at each depth for each treatment and measurement day. A comparison of the mean TDR-derived SWC plotted every hour and the GPR SWC values measured weekly at different depths at the R_{UT} and R_{LT} site is shown in Fig. 4 for the measurement period of 2014 (time series of 2015 and 2016 in Supplemental Fig. S1 and S2). The first row in Fig. 4 shows the precipitation and mean daily temperature data acquired at the weather station close by, whereas the panels below show the mean R_{UT} and R_{LT} SWC results for the sheltered, rainfed, and irrigated plots.

Soil Water Content Time Series of 2014 for the Upper Terrace Rhizotron

The averaged horizontal SWC profiles of R_{UT} are clearly showing an increase in SWC for all depths after major precipitation events such as in June and July 2014. After the rain events, the change in SWC values for the rainfed and irrigated plots is similar (~5% v/v) but larger for the rainfed plot (10% v/v). Note, for example, the large increase of 18 and 10% (v/v) at the 0.2- and 0.4-m depths, respectively, in GPR SWC after the large rain event at the beginning of July in the rainfed plot. The irrigated plot already had a higher SWC compared with the other two plots before the rain event because of two previous irrigations. For the sheltered plot, only a small increase in SWC for the July event can be observed because of the applied shelter on top of the plot. Note that one irrigation in the sheltered plot was necessary at the beginning of June to prevent wilting of the plants. After harvesting of the winter wheat in mid-July, no shelter or irrigation was applied, and the three different plots show a similar trend and behavior. Analyzing these graphs, no immediate relation or dependence between SWC dynamics and crop stage can be noticed. The impact of the precipitation and drying events decreased with increasing depth. The changes in weather conditions can be recognized close to the surface; with increasing depth, the variations are less intense. Special care needs to be taken in interpreting the variability and the quantification of the GPR SWC at the 0.2-m depth (also compare with the synthetic studies in the appendices). Especially for dry conditions, a possible critically refracted air–direct wave interaction could be present. But generally, the 0.2-m depth data follow similar trends as the other depths. Similar observations were made for 2015 and 2016 (Supplemental Fig. S1 and S2).

Table 2. Estimated Fresnel zone radius (R_{FR}) and sampling volume (SV) for the upper terrace (R_{UT}) and lower terrace (R_{LT}) rhizotrons for a range of relative permittivity (ε_r) values. For all calculations, a center frequency of the measured data (f_c) of 170 MHz was used, and the associated wavelength (λ) was obtained.

	R_{UT}				R_{LT}			
Condition	ε_r	λ	R_{FR}	SV	ε_r	λ	R_{FR}	SV
		—— m ——		m^3		—— m ——		m^3
Dry	4	0.88	0.46	0.53	7	0.67	0.39	0.35
Wet	10	0.56	0.35	0.26	20	0.39	0.29	0.17
Intermediate	7	0.67	0.39	0.35	14	0.47	0.32	0.21

Soil Water Content Time Series of 2014 for the Lower Terrace Rhizotron

The SWCs at R_{LT} are generally higher than at R_{UT}, which can be related to a shallower water table in the lower part of the Selhausen test site and the finer soil texture and lower stone content at R_{LT}. For example, the maximum SWC of about 0.4 was obtained for the R_{LT} irrigated plot, whereas the maximum for the R_{UT} for the depth between 0.4 and 1.2 m was around 0.24. Similar to the R_{UT}, an increase and decrease of the GPR SWC can be observed for R_{LT} after rain and dry periods, respectively. An increase in the SWC with increasing depth can be noticed. For the depth below 0.3 m, the smallest SWC is about 0.17, indicating that the soil hardly dries out. For the large rain event in July, an increase in the SWC for all the depths and plots and a SWC increase of up to 0.15 can be observed.

Direct Comparison between GPR and TDR Soil Water Content Results

Figure 5 shows a cross plot between the mean SWC derived from the horizontal GPR measurements and the mean of the SWC measured by TDR. Note that the TDR mean was calculated from the four sensors at each depth (see Fig. 2a) that are closest in time to the GPR measurements for both sites from 2014 to 2016. Based on these data, correlation coefficients r for R_{UT} and R_{LT} were estimated for each year separately and for all 3 yr together and are listed in Table 3, whereas corresponding regression lines are plotted in Fig. 5. The regression lines for both facilities show that there is a bias between the TDR and GPR SWCs, with TDR showing larger SWC than GPR, and

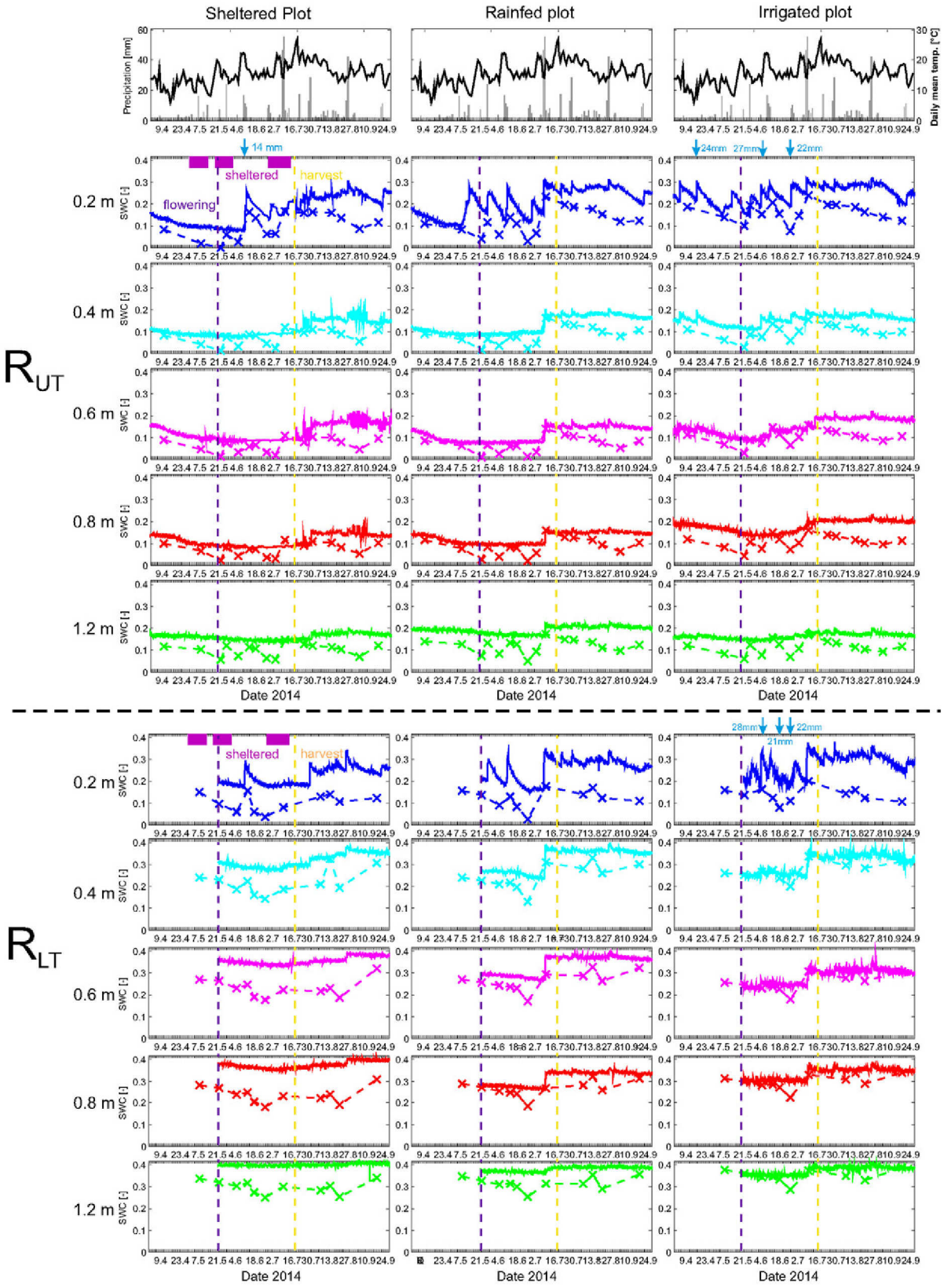

Fig. 4. Comparison of the temporal and spatial mean soil water content (SWC) of the upper terrace (R_{UT}) and lower terrace (R_{LT}) rhizotrons derived by ground-penetrating radar (crosses) and time-domain reflectometry (TDR) sensors (solid lines) for 0.2- and 1.2-m depths using the 2014 data. Averaged horizontal SWC profiles were derived with the three-phase CRIM model. The top row shows the precipitation data obtained by pluviometer (gray bars) and the mean daily temperature (black solid line). Sheltered, flowering, and harvest times are marked as violet boxes, purple dashed lines, and orange dashed lines, respectively. Irrigation events are indicated with blue arrows with the corresponding amount. Note that the date of the year (*x*-axis label) is given with the first and second numbers as day and month, respectively.

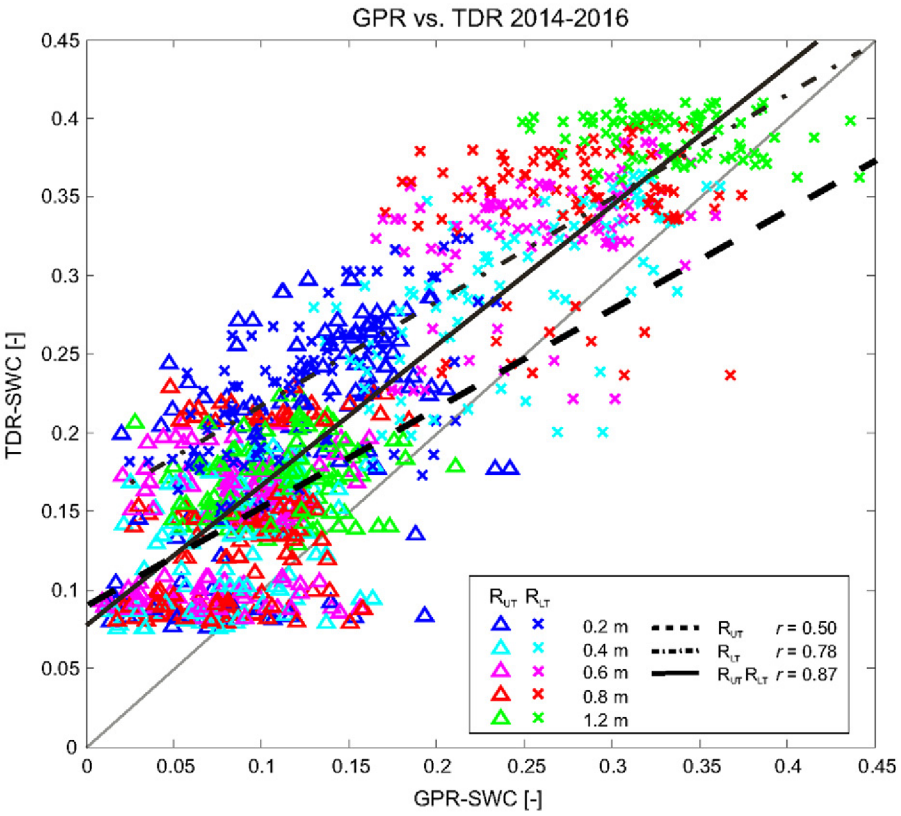

Fig. 5. Comparison of soil water content (SWC) estimated for both the upper terrace (R_{UT}) and lower terrace (R_{LT}) rhizotrons using time-domain reflectometry (TDR) and ground-penetrating radar (GPR) measurements for 2014 to 2016. Each color represents a different depth of investigation. Corresponding regression lines for only R_{UT}, R_{LT}, and combined R_{UT} and R_{LT} are indicated with dashed, dotted, and solid black lines, respectively.

this bias is larger for smaller water contents. This bias could have several reasons. A first explanation could be the different SV of the GPR and TDR measurements. Since the TDR sensors are always at the same location, the deviation between the GPR and TDR SWC should reflect a difference due to variations in local soil properties and local root water uptake that do not lead to complete random deviations with time. While similar trends with time can be seen (Fig. 4; Supplemental Fig. S1 and S2), the GPR SWCs show more variability at deeper depths than the TDR SWCs. For example for the R_{UT} site, except for the large precipitation event in the middle of July, only minor changes in TDR SWC can be observed in the subsoil below the 0.3-m depth, whereas the GPR SWCs reacted also to smaller rain events. These reactions could be caused by preferential flow events that were, by coincidence, not observed in the small sampling volume of the TDR sensors but were detected in the larger GPR sampling volume. In this way, the GPR captures SWC changes that are controlled by heterogeneous structures at a larger scale, which could also include preferential flow patterns (indications seen during infiltration experiments) and different local SWC variability (see Fig. 6). Due to the larger SV, the GPR data can also be affected by shallower SWC changes that react faster to precipitation events. The difference in SV could also cause a bias when TDR probes are installed in zones that are consistently wetter or consistently drier than the soil volume that is sensed by GPR. However, it would be expected that such a bias would be random among the different treatments or different soil depths. This hypothesis is evaluated below when the spatial variation in the observed SWCs is discussed. Another reason for the noise could be the impact of the processing steps of the GPR signals that were adapted for each measurement day and soil plot. Looking at Fig. 4, it seems that the deviations between GPR and TDR measurements are correlated for a certain observation day and facility for all depths and treatments. To what extent this is related to the signal processing requires further investigation.

Table 3. Correlation coefficient *r* between time-domain reflectometry and ground-penetrating radar derived soil water contents for the upper terrace (R_{UT}) and lower terrace (R_{LT}) rhizotrons in 2014 to 2016.

	R_{UT}				R_{LT}				$R_{UT} + R_{LT}$
Treatment	2014	2015	2016	2014–2016	2014	2015	2016	2014–2016	2014–2016
Sheltered	0.65	0.66	0.19	0.57	0.89	0.82	0.86	0.86	0.91
Rainfed	0.78	0.71	0.59	0.66	0.89	0.80	0.87	0.81	0.88
Irrigated	0.73	0.54	0.30	0.19	0.76	0.72	0.89	0.77	0.85
All plots	0.76	0.68	0.58	0.50	0.77	0.75	0.82	0.78	0.87

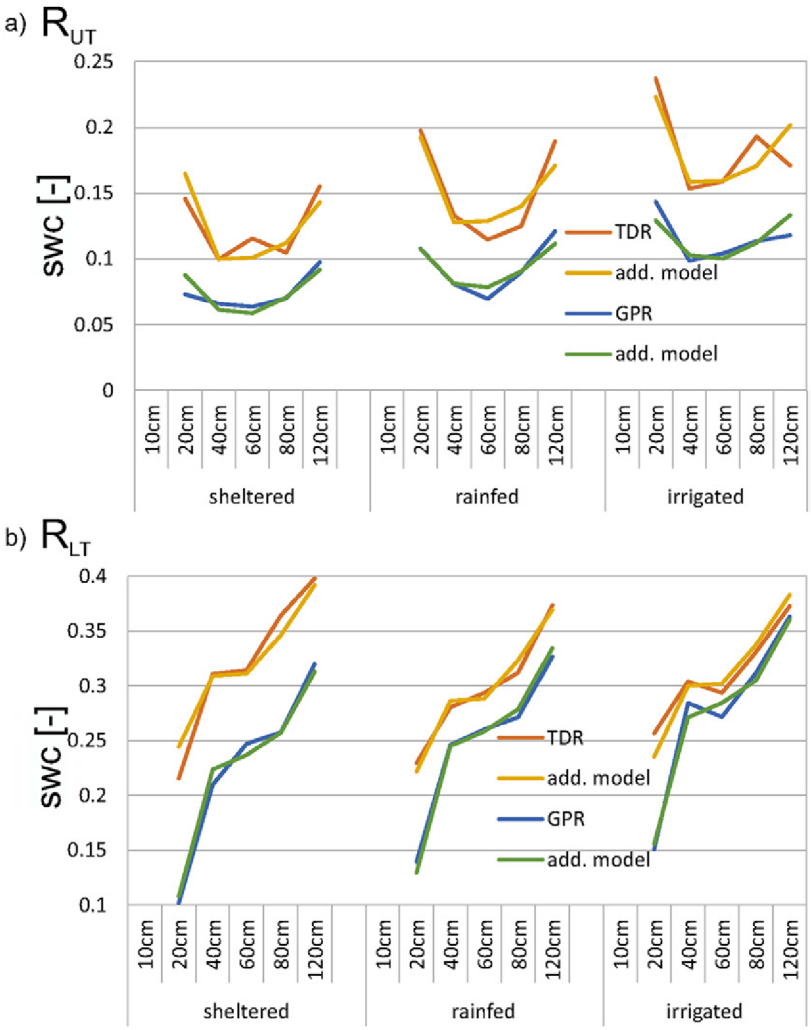

Fig. 6. Time-averaged water contents during the winter and summer wheat growing seasons (1 April–harvest) in 2014, 2015, and 2016 in (a) the upper terrace rhizotron (R_{UT}) and (b) the lower terrace rhizotron (R_{LT}) for different water treatments and depths derived from time-domain reflectometry (TDR) and ground-penetrating radar (GPR) measurements and calculated using the additive model.

Finally, it needs to be mentioned for the installation of the TDR probes in R_{UT}, the larger stones (with diameters >30 mm) were excluded from the material that was packed around the soil sensors, whereas the gravimetric fraction of coarse fragments (with diameter >2 mm) was kept similar to guarantee a good coupling. This could have resulted in an higher water retention and hence higher SWCs that were measured with TDR than with GPR (Cai et al., 2016). However, this does not explain the bias that was observed at R_{LT} where the probes were inserted in the soil.

To evaluate the SWC measurements in the different facilities, at the different depths, and for the different water treatments, we calculated time averages of the measurements during the three wheat growing periods (1 April–harvest). A simple additive model of the water treatment and depth effects was set up:

$$SWC_{i,j} = SWC_{\cdot,\cdot} + \Delta SWC_{water i,\cdot} + \Delta SWC_{\cdot,depth j} + E_{water i,\, depth j} \quad [3]$$

where $SWC_{\cdot,\cdot}$ is the overall averaged SWC for all depths and water treatments in a given facility, $\Delta SWC_{water i}$ is the effect of the ith water treatment (i = sheltered, rainfed, or irrigated), which is calculated from the difference between the average SWC at all depths for the ith treatment and the overall average, $\Delta SWC_{\cdot,depth j}$ is the effect of the depth, which is calculated from the difference between the average SWC for all treatments at the jth depth and the overall average, and $E_{water i,depth j}$ is an error term that represents the interaction effect between the ith water treatment and jth depth, effects of soil heterogeneity, and measurement errors. In Supplemental Table S1, the mean SWC and the effects are given. In Fig. 6, time-averaged SWCs for the different water treatments and depths in the two facilities that were measured with GPR and TDR and that were calculated using the additive model are shown. The additive model with error term presumes that the effect of the water treatment is the same for all depths and that the effect of the depth is independent of the water treatment. This implies that the SWC profiles with depth that are predicted by this model shift with a constant value among the different treatments (see Fig. 6).

The time, depth, and water treatment averaged water contents $SWC_{\cdot,\cdot}$ indicate that the TDR measured values are about 6% (v/v) higher than the GPR measurements in both facilities. The SWCs in the stony soil of the upper facility are on average 16% (v/v) lower than in the silty soil of the lower facility. Looking at the water treatment effects, the GPR measurements show that in both the upper and lower facilities, the sheltered plots were drier than the rainfed plots and irrigated plots, as expected. For the upper facility, the TDR measurements show similar water treatment effects as the GPR measurements, but for the lower facility, the TDR measurements indicated a wetter soil in the sheltered treatment than in the other treatments. This indicates a systematic difference in soil properties of the TDR measurement sites in the sheltered, rainfed, and irrigated plots of the lower facility. The topsoil in the upper facility has a lower stone content than the subsoil, which is reflected in a higher SWC in the topsoil layer (this is further confirmed by the SWCs measured by TDR probes at the 0.1-m depth, which are not shown here). For R_{LT}, the soil profile is on average the driest at 0.2 m, and the SWC increases with depth. The difference between the additive model and the time-averaged SWC for a certain water treatment and depth correspond with the interaction-error term E. For R_{UT}, both TDR and GPR measurements show a negative interaction at the 0.2-m depth and a positive one at the 1.2-m depth for the sheltered plot and opposite interactions in the irrigated plot. This demonstrates that root water uptake, which dries out the soil, and irrigation

and rainfall, which wet up the soil, have a stronger impact in the upper soil layer and a smaller impact in the subsoil. Of note is that both GPR and TDR show lower SWCs at the 1.2-m depth in the irrigated than the rainfed plots, which indicates the effect of soil heterogeneity on the SWC measurements in these plots. For the lower facility in the silty soil, the TDR-measured SWCs show similar interactions as in the upper facility, but the GPR measurements show smaller or opposite interaction effects. The reason for the interactions in the TDR measurements could be the underestimation of the SWC in the deeper soil layer of the rainfed and irrigated plots by TDR sensors that were installed in an apparently drier region of the plot (see Fig. 7).

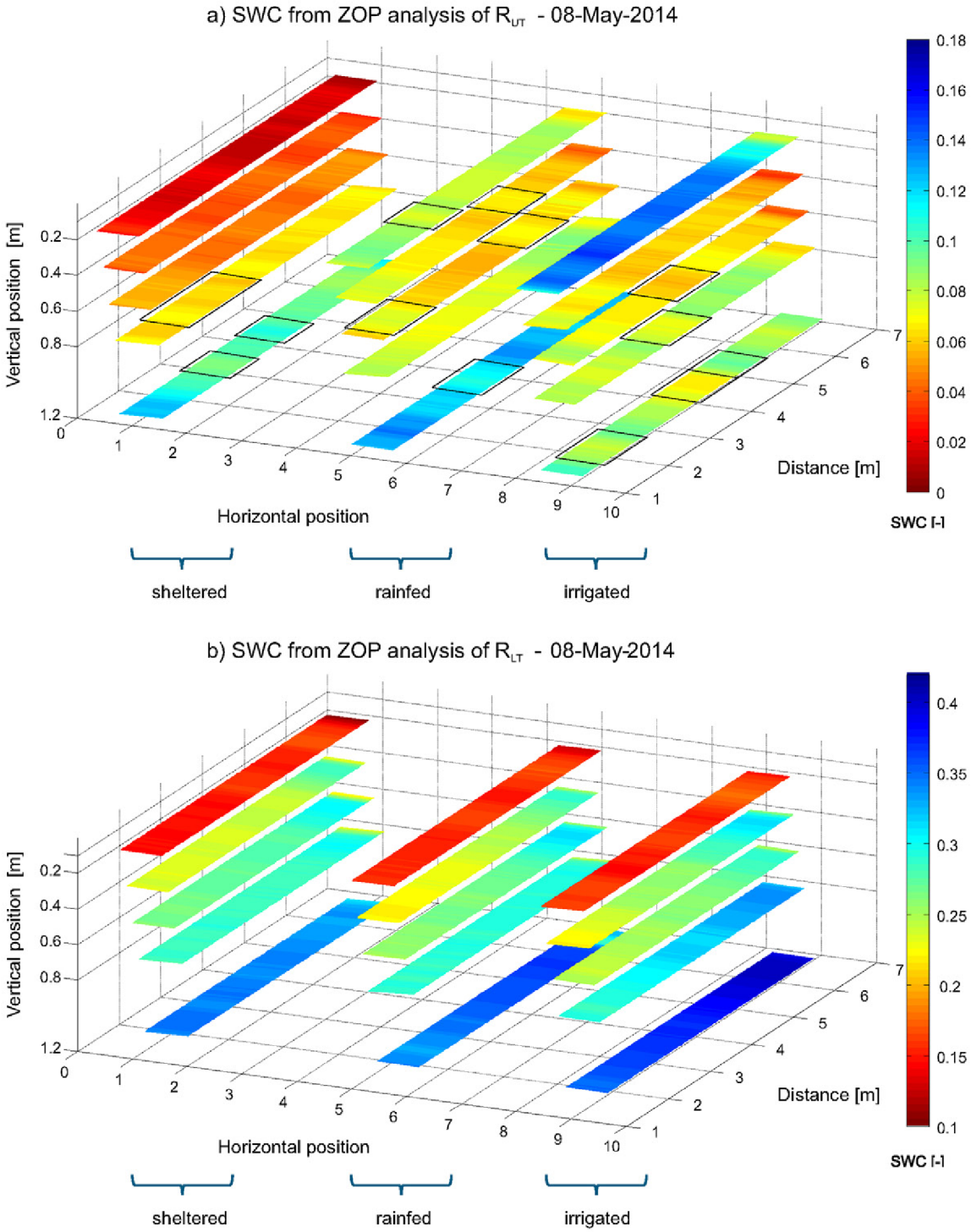

Fig. 7. Horizontal and lateral soil water content (SWC) variability as determined by zero-offset profile (ZOP) analysis for (a) the upper terrace rhizotron (R_{UT}) and (b) the lower terrace rhizotron (R_{LT}). Horizontal SWC profiles after CRIM using the 8 May 2014 data for all three treatments: sheltered, rainfed (natural condition), and irrigated. Each measurement point (5-cm spacing) is color coded with the corresponding SWC. Note the different color bars of the SWC. The black outlined boxes indicate patches of higher or lower SWC that were consistent with the time during the 3 yr.

Based on these analyses, we can conclude that GPR- and TDR-measured and time-averaged SWC in different soils, at different depths, and for different water treatments were generally consistent with each other. However, there was a clear bias between the two measurements, with TDR giving higher SWCs than GPR. Also, inconsistencies could be observed and some of them could be related to the spatial variability of the soil properties within and between the plots. Therefore, we next discuss the behavior of the GPR SWC along the tubes to analyze the spatial variability in more detail.

GPR Soil Water Content Variability

Semi-Three-Dimensional Soil Water Content Images of the Rhizotrons

For each measurement day, the SWC values of the GPR measurements were estimated for all positions (every 5 cm) along the horizontal boreholes for five depths and three treatments. The obtained SWC values were then plotted as slices in between the horizontal boreholes for each depth level at five depths for the three treatments such that a semi-three-dimensional image was obtained of the 1.2-m-depth by 9-m-width by 6-m-length volume for the R_{UT} and R_{LT}. Figure 7a and 7b show the obtained SWC on 8 May 2014 for the R_{UT} and R_{LT}, respectively, where the SWC values located in the first meter close to the trench were excluded because of the presence of sensors. For this date, an increasing SWC with depth is visible for both facilities except the irrigated plot at R_{UT}. It can be noted that the vertical variability in SWC is significantly larger than the horizontal, although the horizontal SWC variability is still significant at all depths. Particularly remarkable is the large contrast between the topsoil (uppermost layer) and the subsoil. As expected, the sheltered plot shows lower SWC values than the rainfed and irrigated plots, while the irrigated plots show slightly higher SWC than the rainfed ones.

The mean and corresponding standard deviation (SD) for each depth and treatment for the data from 2014 to 2016 can be seen in Fig. 8. Every point represents the mean and SD of one ZOP crosshole measurement along a pair of 6-m boreholes during a measurement day. The R_{UT} SD reaches maximum values of 0.02, and the mean SWC is mostly <0.2 (except for the 0.2-m depth). Except for the lowest depth in the R_{UT}, the sheltered plots show a smaller SD than the rainfed and irrigated plots. The R_{LT} SD reaches a maximum value of 0.03 and, for the 1.2-m depth, even 0.04. The mean R_{LT} SWC for depths between 0.4 and 1.2 m shows minimum values of about 0.1 and maximum values of about 0.4, whereas for the shallow depth of 0.2 m, a minimum value close to zero and maximum values up to 0.25 were obtained. Overall, more variability and scatter of the relation between the mean and SD of the SWC for all plots and depths can be observed for R_{LT} than R_{UT}. This could be partly due to deviating boreholes present in R_{LT}.

Spatial and Temporal Variability of GPR Soil Water Content after Rain Events

For a more detailed illustration and characterization of the spatial and temporal variability of SWC for the large rain event

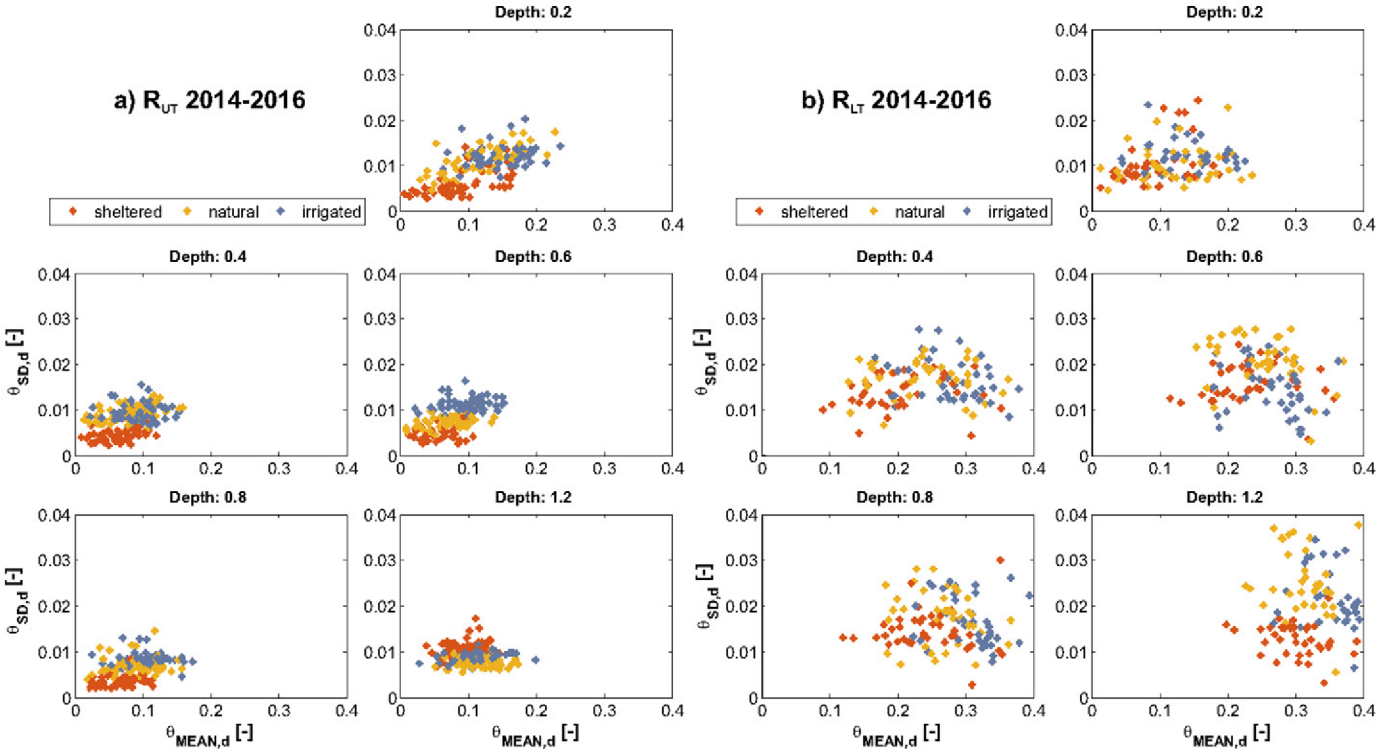

Fig. 8. Mean soil water content (SWC) for each depth and the corresponding standard deviation (SD) for (a) the upper terrace rhizotron (R_{UT}) and (b) the lower terrace rhizotron (R_{LT}) for the time series 2014 to 2016. The different treatments are indicated with different colors.

in July , the rainfed plot is analyzed in more detail in Fig. 9. The times series between 26 June 2014 and 24 July 2014 shows the highest variability of the SWC between dry and wet conditions as a response to the major rain events that took place between 8 and 10 July 2014 (Fig. 9). We observed an increase of 0.1 in SWC for the subsoil below the 0.3-m depth, while for a depth of 0.2 m, the increase in SWC was approximately 0.16, probably due to the higher porosity. For comparison, the mean of four TDR measurements at the same time as the GPR measurements are plotted. Although the absolute values are higher, the general trends of increasing and decreasing SWC are present for both. Figure 9b shows the vertical SWC profiles with time for the same dates, where it clearly can be seen that the rain events caused an increase in SWC for all depths with time, while in between the rain events the SWC decreased (indicated by the arrows on top). In Fig. 9a, a general increase of the SWC and also an increasing vertical SWC variability can be observed within the red ellipses for the first 3 d, which can also clearly be observed in Fig. 9c, where the lateral variability for these 3 d at five depths is shown. Here also the consistent patches that remained either wetter or drier during and after the infiltration event can be identified.

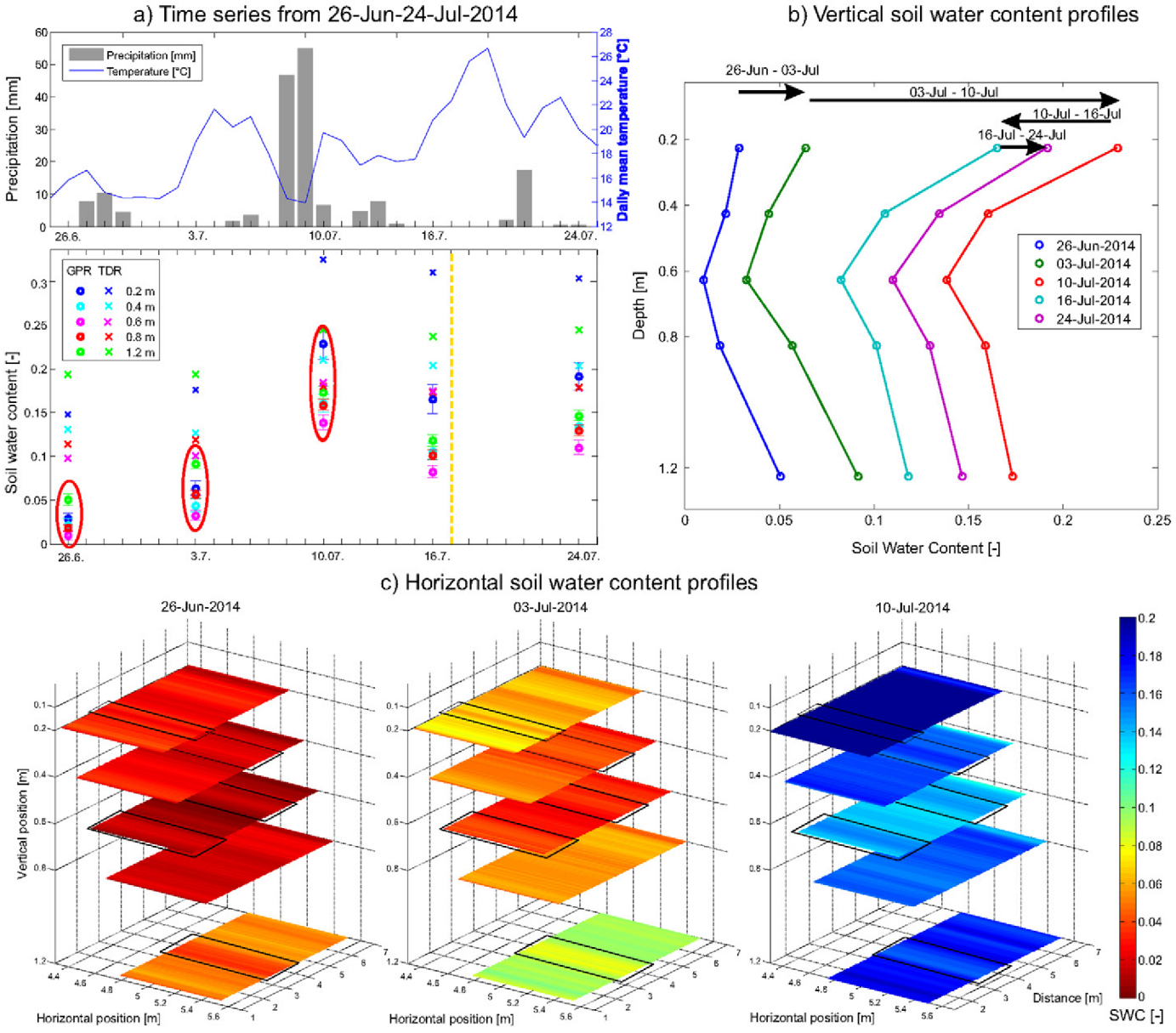

Fig. 9. Detailed analysis of the soil water content (SWC) distribution for 26 June to 24 July 2014 for the rainfed plot of the upper terrace rhizotron (R_{UT}): (a) daily precipitation, mean temperature, and time series of the SWC for depths of 0.2, 0.4, 0.6, 0.8, and 1.2 m derived by time-domain reflectometry (TDR) and ground-penetrating radar (GPR) as crosses and circles, respectively, with the harvest date indicated by the yellow line (note that the date of the year [*x*-axis label] is given with the first and second number as day and month, respectively); (b) vertical GPR SWC for 26 June to 24 July 2014; (c) horizontal depth slices of the SWC for the 3 d marked in (a) by the red ellipses showing dry, intermediate, and wet conditions. The black outlined boxes indicate the SWC patches that were consistent with time (see Fig. 7).

Spatial Variability along the Rhizotubes

To investigate the consistency of the lateral SWC variability, we plotted the SWC variability of the different measurement days in 2014 with gray lines in Fig. 10. After subtracting the mean SWC at each depth from the individual SWC along the tubes for all measurement days separately for the 3 yr of investigation, the mean of all these gray lines (solid black lines) provide a mean horizontal SWC variability for 2014. Similarly, the mean horizontal

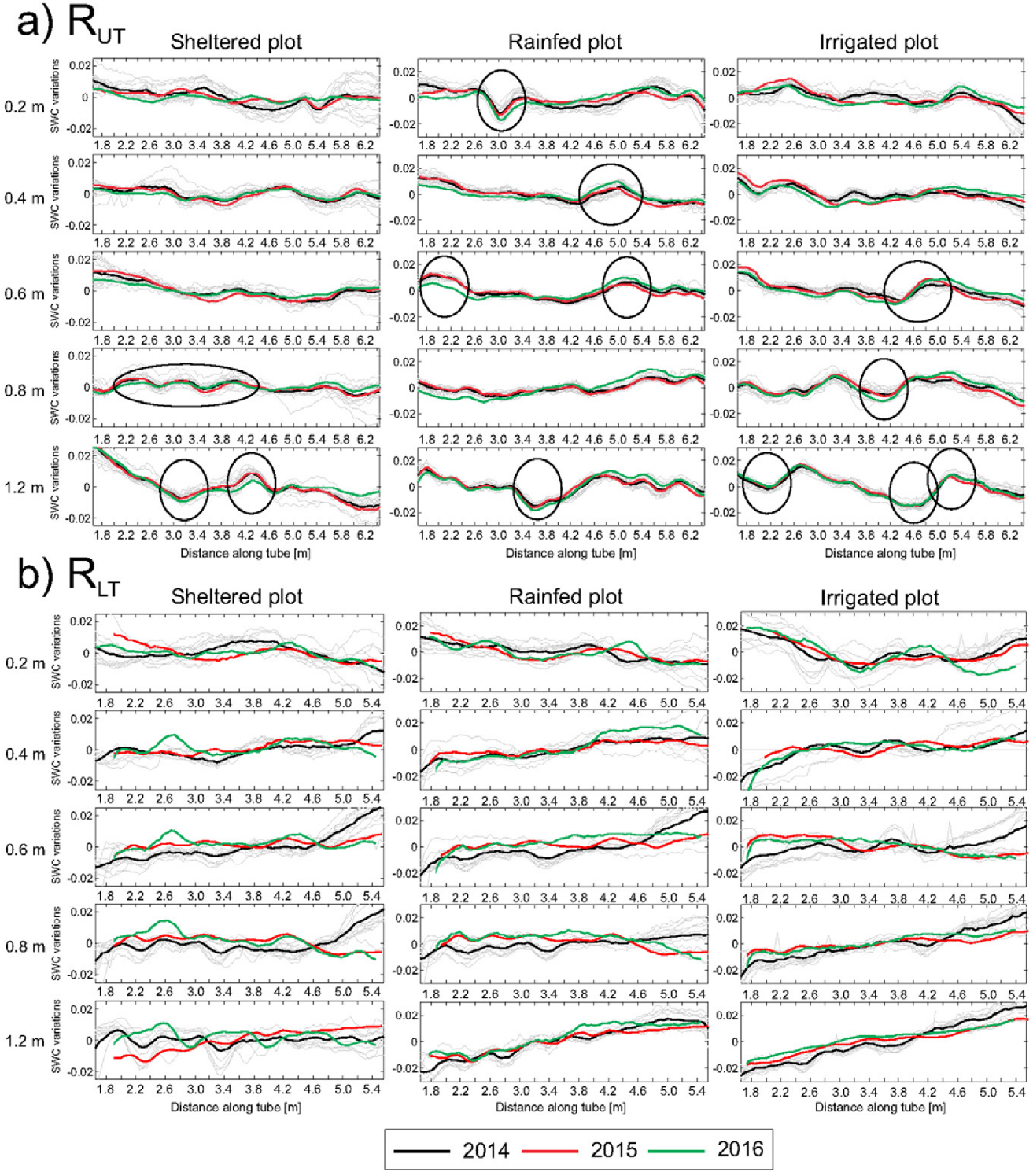

Fig. 10. Detailed analysis for (a) the upper terrace rhizotron (R_{UT}) and (b) the lower terrace rhizotron (R_{LT}) of the soil water content (SWC) depth slices. The mean SWC of each depth slice was subtracted from the individual SWC values along the depth slices. The gray lines represent the individual SWC profiles for all the measurement days of 2014. The solid black, red, and green lines represent the means of all the measurement days of the years 2014, 2015, and 2016, respectively. The black circles indicate the higher and lower SWC patches that were consistent with time (see Fig. 9) along the horizontal slices.

SWC variability for 2015 and 2016 are indicated by the red and green lines, respectively. In particular for R_{UT}, the site with the higher gravel content and coarse material, very clear and consistent patches during the 3 yr can be seen (Fig. 10a, black circles). Furthermore, these consistent structures with time also indicate the repeatability and reproducibility of the GPR data analysis. This observation suggests that the SWC variability of R_{UT} is probably controlled by the soil properties rather than root growth of the wheat and indicates heterogeneity of the soil properties along the tubes. For the R_{LT}, the site in the more silty soil, the SWC variability of R_{LT} in the gray 2014 profiles shows similar trends but a much larger spread. Contrary to R_{UT}, the mean R_{LT} SWC curves for 2014, 2015, and 2016 show also larger differences. This could be the result of varying root water uptake along the tubes during the different years. Note that some results show a clear increasing trend from low to higher SWC (e.g., the 1.2-m depth of the irrigated and rainfed plots). This might reflect horizontal variations in SWC and suggests that the TDR sensors at the 1.2- and 0.8-m depths in the irrigated and rainfed plots are located in a drier part of the plot and might explain why the TDR sensors in the rainfed and irrigated plots show smaller SWC than in the sheltered plot at R_{LT}. However, the persistent increase in SWC along the tubes might also be caused by the horizontal boreholes having some deviation from the planned 0.75-m distance due to the horizontal drilling. Since for R_{UT} the tubes were buried and not drilled, such deviations are not expected at R_{UT}. The boreholes are straight along the 7-m length (checked after drilling), but an unknown error in the angle of the tubes could be present. If we consider, for example, a maximum deviation away from the 75-cm offset from ±5 cm (±10 cm) at the end of the tube for the average soil condition of R_{LT} ($\varepsilon_r = 14$), the SWC would vary by ±3 (±6)% (v/v) SWC. This makes clear that a very detailed deviation logging needs to be performed to investigate this effect on the SWC in more detail, especially for R_{LT}. The reason why the R_{UT} shows a small spread and similar trends over the years whereas R_{LT} shows a larger spread and different trends is not clear and might be due to the different textures of the soil material.

Water Content Spatial Distribution for Different Crop Types

In 2017 maize, instead of wheat, was sown. Note that the shelter was removed and, for 2017, two rainfed plots were present. The same analysis for the 2017 GPR data was applied as for the other years of both facilities. While the wheat showed no clear impact on the GPR recordings, the maize plants showed an impact, especially under dry conditions at R_{UT} (boxes in Fig. 11). In particular during the growing phase of the plants between July and August, clear patches of where the plants are located can be observed. For example, for very dry conditions during the growing phase such as 27 July 2017, a higher SWC can be seen at the locations of the maize rows (very dry soil), and this contrast decreases with increasing depth. The measured SWC shows peaks with a separation of about 75 cm, which equals the distance between the crop rows (Fig. 11, right side). Ten rows were planted along the rhizotube profiles, of which seven can be detected with the GPR data. After some rain events at the end of July, the GPR SWC data of 2 Aug. 2017 also show patches but this time not that clearly. Furthermore, the SWC is lower at the maize plant rows (greatest for the irrigated plot). Therefore, the ZOP recordings and the inferred SWC variations are influenced by not only the weather conditions and the soil but also by the presence of the crop. This becomes clear also by analyzing the SWC variation along the 7-m-long tubes for the time period from July to August (Fig. 11, left side). For a dry day (cyan line), a very strong variation is visible with maximum peaks at the plant locations. By comparing these variations with Fig. 7c, where constant patches with time for wheat were visible, for maize these constant patches overlap and are controlled by the plant presence during the growing phase and more temporal changes are observed. One explanation could be that under very dry soil conditions, the SWC below the plant rows was higher than between the rows and this could be caused by the amount of water in the plant roots in combination with the higher root density below the plant row. These variations along the depth slices were already visible in the unprocessed data (not shown). As Fig. 11 indicates, the SWC patterns caused by the root zone are visible only in the shallow depths. The roots are very concentrated near the surface and are more distributed with increasing depth (Fig. 12). This is particularly true for R_{UT} with a high root count density near the surface. For R_{LT}, high root count density values are distributed across the entire depths (patches much harder to identify in the GPR data, not shown). Note, that the effects of the surface and aboveground plant biomass (see Table 2 for sensing volume) is currently not clear and needs to be investigated in future research.

Summarizing, for plants like maize, clearly the strength of the GPR SWC estimation is visible due to its power to sense lateral SWC changes and distribution. We have seen that a clear link between the SWC of the GPR and the plant location can be made. Such variations could maybe also have been shown for the upper few centimeters with TDR sensors, but to gain the same spatial resolution, a large number of sensors would need to be installed, which would disturb the soil conditions. More research is necessary to link the measured SWC from GPR to the SWC of the roots themselves. Generally, the currently estimated SWC is an averaged value for a certain domain including all components, e.g., soil, roots, and air. Interestingly, other studies that mainly conducted ERT measurements suggested an opposite row–interrow effect of the SWC in a maize crop, with a smaller SWC under the rows (e.g., Michot et al., 2003; Garré et al., 2013). It must be noted that ERT does not measure the permittivity, and the impact of root water content on bulk soil electrical conductivity is not unequivocal.

Conclusions and Outlook

We used a novel experimental setup to map and monitor SWC variability and dynamics using horizontal crosshole GPR data

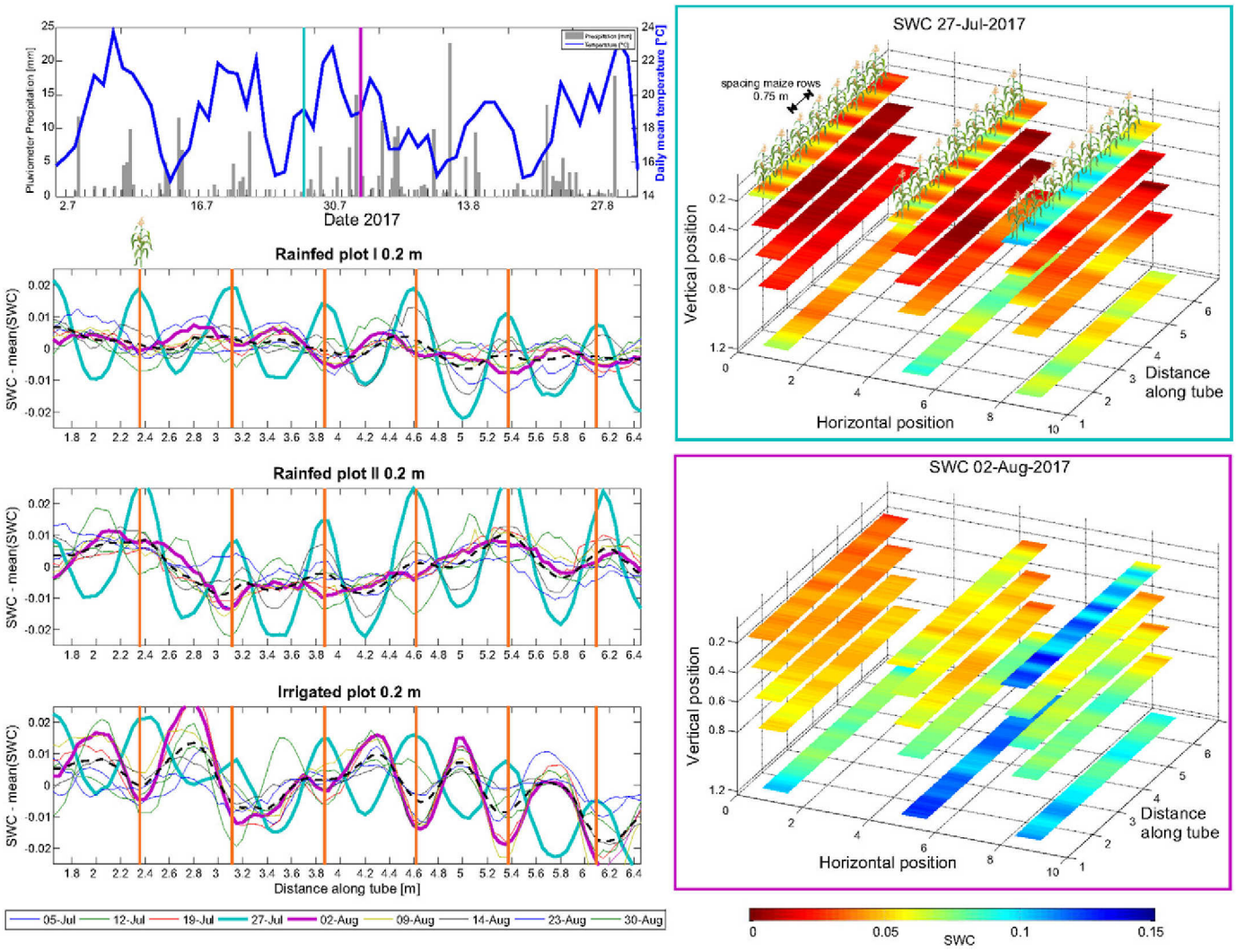

Fig. 11. Detailed analysis for (a) the upper terrace rhizotron (R_{UT}) for the soil water content (SWC) in the presence of maize in 2017: weather conditions and the SWC variations (similar to Fig. 6) at the shallow depths for all three plots for the main growing period between July to August, with orange lines indicating the position of the maize plant along the tubes (left) and horizontal SWC profiles after CRIM for R_{UT} for two example dates during the growing phase for all three treatments: rainfed I (previously sheltered), rainfed II, and irrigated (right).

in two minirhizotron facilities, R_{UT} and R_{LT}, in the upper and lower terraces, respectively. The setup allowed monitoring spatial and temporal variations in SWC variability caused by precipitation, different treatments (sheltered, rainfed, and irrigated), crops (wheat and maize), and soil types (gravelly soil and clayey–silty soil) during four growing seasons and under bare field conditions. More than 150 time-lapse GPR days of measurements were performed. We generally found higher SWC values at R_{LT} than at R_{UT} due to the presence of a water table and the finer textured soil material. At both locations, the vertical variability in SWC was significantly larger than the horizontal one. We observed a clear effect of the treatments on the SWC. The sheltered plot showed lower SWC values than the rainfed and irrigated plots, while the irrigated plots showed slightly higher SWC than the rainfed ones. For R_{UT} with the higher gravel and sand content, much more horizontal variability in SWC was noticed compared with R_{LT}. Mapping the spatial variability of the SWC along the depth slices along the boreholes indicated, especially for R_{UT}, time alternating patches with lower and higher SWC (±0.02). The cause of these patches needs to be investigated in more detail and might be due to heterogeneous structures that could be related to preferential flow paths. To better quantify and illustrate the behavior of the spatial variability and to improve the investigation of wetting and drying of the identified patches along the depth slices, higher temporal sampled data from climate-dependent GPR measurements are required than the weekly measured data presented here, especially during major precipitation events.

Comparison of the GPR SWC with TDR SWC values showed similar trends with time but consistently lower GPR SWC values. These differences between the TDR and GPR measurements can most likely be explained by different measurement volumes and spatial heterogeneity. Due to interfering critically refracted air wave and direct subsurface waves, it was not possible to map the shallow SWC values at the 0.1-m depth with GPR using

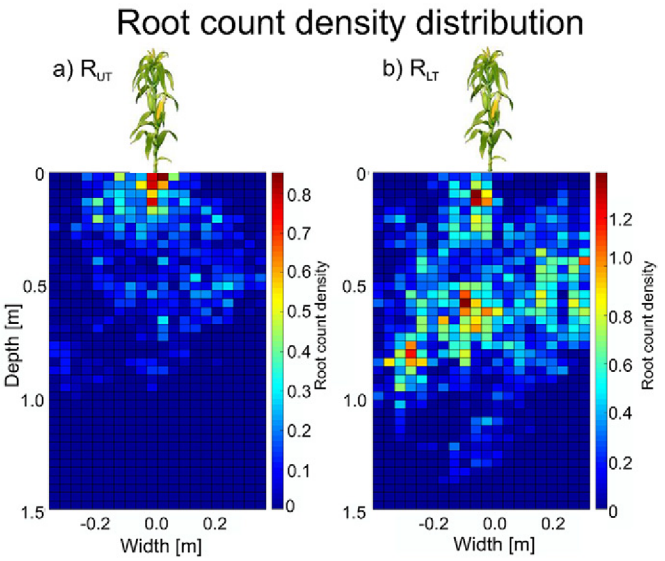

Fig. 12. Root count density distribution for maize after the growing phase measured in a grid of 0.0375 by 0.0375 m for (a) the upper terrace rhizotron (R_{UT}) and (b) the lower terrace rhizotron (R_{LT}). The data were acquired by excavating a trench close to the maize plants and counting the number of roots per grid cell (two replicates per site).

first break picking. More sophisticated methods such as full-waveform inversion approaches are needed that are able to model the entire GPR trace including these interferences (Klotzsche et al., 2016). Further, two uncertainties in the SWC estimates are discussed that could influence the SWC: (i) a possible deviation of the tubes away from the assumed offset of 0.75 m that is currently not considered (mainly for R_{LT}) and (ii) the assumptions of the CRIM parameters to calculate the SWC. Further work needs to involve accurate and detailed deviation measurements of the boreholes and laboratory studies to better define the CRIM parameters.

In contrast to TDR, crosshole GPR was able to detect differences in the spatial variation in SWC in the horizontal direction between maize and wheat. A major advantage of GPR-based measurements compared with TDR is the fact that it may provide detailed information on the spatial and temporal variation of SWC in the subsurface. Our crosshole GPR setup in combination with rhizotron facilities allowed the effect of crop and treatment differences on the spatial and temporal variation of SWC to be studied and may therefore be extremely useful for investigating root water uptake processes as a function of soil and crop type. In addition, the long-term time-lapse GPR data can be used to derive relevant hydraulic properties such as the Mualem–van Genuchten parameters for both facilities and hence different soil types (e.g., Rossi et al., 2015; Busch et al., 2013), where also the influence of the growing plants including roots can be incorporated. In this way, high spatial resolution investigations can be performed to study the soil–plant–atmosphere interactions of agricultural crops at the field-plot scale. To disentangle the SWC estimates from the root system and the soil properties from the GPR SWC, more research is needed, e.g., bare-soil field conditions can help to investigate the soil structures before sowing and after harvest. Furthermore, special care needs to be taken in the data analysis for very dry soil conditions.

Appendix A

Synthetic Study: GPR Wave Interference Close to Surface

We defined a two-layer three-dimensional model and computed the EM wave using the three-dimensional finite difference time domain solver gprMax (Warren et al., 2016), where the air layer with permittivity $\varepsilon_r = 1$ was overlying a soil layer of $\varepsilon_r = 5$ (dry sand). We calculated the EM field components for the same depth positions and spacing of the transmitter and receivers that are present at the rhizotron facility. For comparison, we also modeled the electrical field in a homogenous medium with a permittivity of $\varepsilon_r = 5$ (Fig. A1a). For all the synthetic models, the conductivity σ was chosen to be constant at $\sigma = 10$ mS/m for the soil; as a source pulse we used a Ricker wavelet using a center frequency of 200 MHz. The results indicate that the influence of the interferences of air and direct waves on the first breaks is largest at the 0.1- and 0.2-m depths (Fig. A1a and A1b). With increasing depth, the air wave interaction features decrease and arrive later as the first breaks of the direct wave of the traces and no interference on the first break is present (Fig. A1a). To investigate the influence of wet and dry soil conditions for the shallowest borehole pair at the 0.1-m depth, the same two-layered model was used with varying soil permittivity from 5 (dry sand) up to 20 (wet sand) and is shown in Fig. A1b. In all the models, a phase shift and an influence of the amplitude on the trace can be observed (Fig. A1b), indicating that first-break picking and ray-based approaches would return erroneous results. To obtain reliable permittivity and SWC results for the shallow boreholes, we need to take this refracted airwave and direct wave interference into account, and a more sophisticated analysis approach like full-waveform inversion (Klotzsche et al., 2016, 2019) needs to be used.

Appendix B

Synthetic Study: First Break Picking Close to Interfaces and Soil Water Content Gradients

To estimate the error of the travel time picking in the presence of interfaces and gradients, additional synthetic models were investigated. Figure B1 shows the different models and the picked permittivities, and a detailed comparison between the picked and true values is shown in Table B1. For Models I and II, the first break picking at the 0.4- and 0.2-m depths shows the largest deviation, with a lower permittivity caused by a refracted wave traveling through the fastest layer with the lowest permittivity. For the increasing and decreasing gradients in permittivity (Models III and IV), relatively good agreement between the model and the picked values was obtained, except for the Model IV topsoil pick at the 0.2-m depth. Model V comprises a high-permittivity zone embedded in a lower permittivity medium. Such a layer can cause a low-velocity

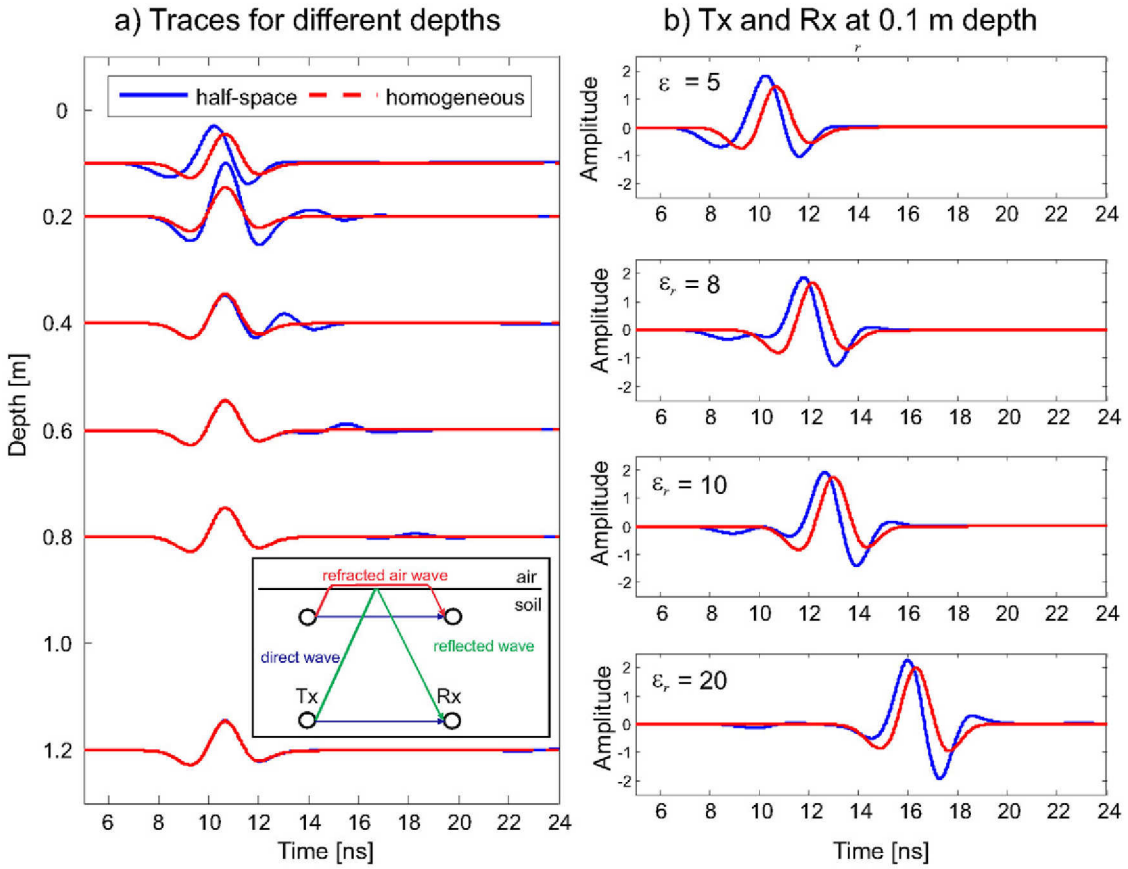

Fig. A1. Comparison of synthetic horizontal borehole traces with a borehole separation of 0.75 m. Traces for a three-dimensional homogenous space with a relative dielectric permittivity (ε_r) of 5 in red and traces for the presence of an air layer on top of the $\varepsilon_r = 5$ of the two-layered medium in blue: (a) traces for transmitter (Tx) and receiver (Rx) depths of 0.1, 0.2, 0.4, 0.6, 0.8, and 1.2 m, with the possible ray paths for a simple two-layered model in the embedded box; and (b) comparison of synthetic traces at the 0.1-m depth for ε_r values of 5, 8, 10, and 20 for the homogeneous and two-layered media.

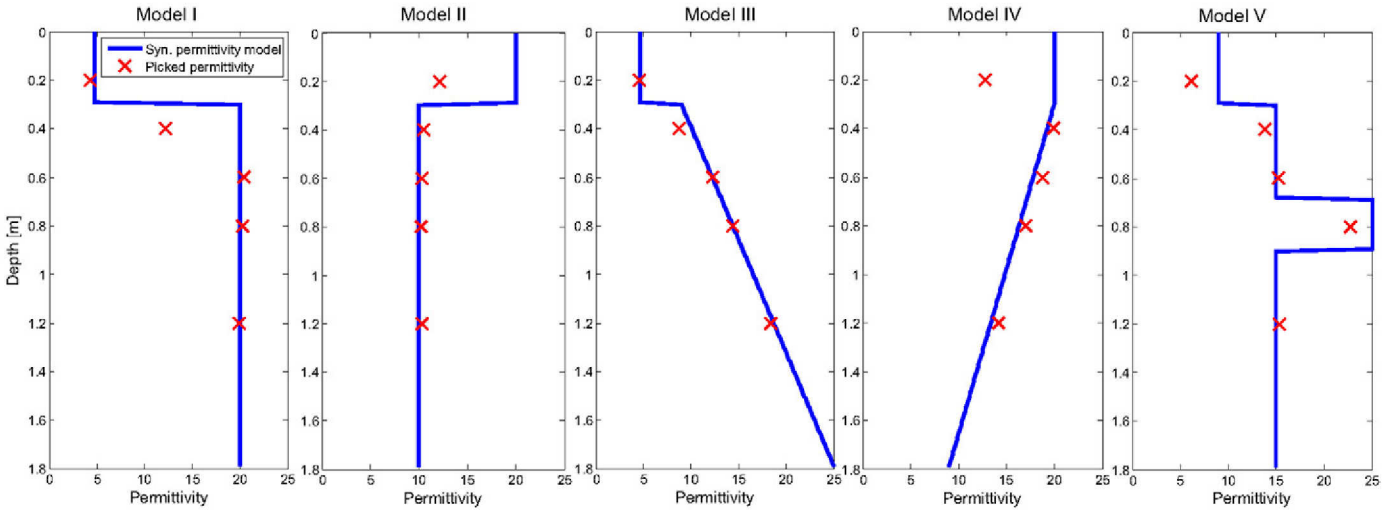

Fig. B1. Different synthetic models with varying permittivity for top- and subsoil (solid blue lines). Synthetic ground-penetrating radar (GPR) traces were generated with gprMax3D. The boundary between top- and subsoil is located at the 0.3-m depth. Models II and III are modeled with a linear gradient of the permittivity in the subsoil. Conductivity is constant for all models at 10 mS/m. For the same depths of the rhizotrons, the first arrival travel times were picked and converted into permittivity (red crosses). Exact values and corresponding differences are illustrated in Table B1.

Table B1. Results of the different synthetic models using gprMax. For Models I to V for each depth between 0.2 and 1.2 m, the relative dielectric permittivity (ε_r) used in the model and the handpicked transformed ε_r are shown. The difference between the modeled and handpicked permittivity values is indicated as $\Delta\varepsilon_r$. The resulting differences in SWC were calculated using Topp's equation (Eq. [2]) and are indicated as $\Delta\theta_{Topp}$.

Depth	ε_r model	ε_r picked	$\Delta\varepsilon_r$	$\Delta\theta_{Topp}$
m				%
		Model I		
0.2	4.70	4.49	0.21	0.52
0.4	20.00	12.23	7.77	11.56
0.6	20.00	20.40	−0.40	−0.49
0.8	20.00	20.29	−0.29	−0.36
1.2	20.00	19.86	0.14	0.17
		Model II		
0.2	20.00	12.12	7.88	11.761
0.4	10.00	10.48	−0.48	−0.932
0.6	10.00	10.30	−0.30	−0.586
0.8	10.00	10.23	−0.23	−0.438
1.2	10.00	10.30	−0.30	−0.586
		Model III		
0.2	4.70	4.61	0.09	0.23
0.4	9.97	8.77	1.19	2.39
0.6	12.11	12.23	−0.12	−0.21
0.8	14.26	14.36	−0.10	−0.16
1.2	18.56	18.40	0.16	0.21
		Model IV		
0.2	20.00	15.60	4.40	6.05
0.4	19.34	19.90	−0.56	−0.71
0.6	17.86	18.60	−0.74	−0.99
0.8	16.38	16.98	−0.60	−0.87
1.2	13.43	13.73	−0.30	−0.50
		Model V		
0.2	9.00	6.69	2.31	4.94
0.4	15.00	14.18	0.82	1.31
0.6	15.00	15.25	−0.25	−0.39
0.8	25.00	22.78	2.22	2.29
1.2	15.00	15.31	−0.31	−0.49

waveguide for EM waves showing distinct wave propagating effects. In previous vertical crosshole studies (e.g., Klotzsche et al., 2013) such zones could be related to zones of higher porosity and zones of preferential flow. The first break picking of the traces for such a layer indicates the presence of a high-permittivity zone, but it underestimates the permittivity and hence the SWC (see Table B1).

Acknowledgments

We thank Max Oberröhrmann, Joschka Neumann, and Normen Hermes for the cooperation, support, and construction of the minirhizotron facilities. We acknowledge the support by the SFB/TR32 "Pattern in Soil–Vegetation–Atmosphere Systems: Monitoring, Modelling, and Data Assimilation" funded by the Deutsche Forschungsgemeinschaft (DFG). Furthermore, we thank the Terrestrial Environmental Observatories (TERENO) for support at the test site and for meteorological data. We thank Ute Wollschläger (associate editor), Andrew Binley (reviewer), and an anonymous reviewer for their constructive reviews. Anja Klotzsche was supported during this study by the Helmholtz Postdoc Programme.

References

al Hagrey, S.A. 2007. Geophysical imaging of root-zone, trunk, and moisture heterogeneity. J. Exp. Bot. 58:839–854. doi:10.1093/jxb/erl237

Allroggen, N., L.M.B. van Schaik, and J. Tronicke. 2015. 4D ground-penetrating radar during a plot scale dye tracer experiment. J. Appl. Geophys. 118:139–144. doi:10.1016/j.jappgeo.2015.04.016

Beff, L., T. Günther, B. Vandoorne, V. Couvreur, and M. Javaux. 2013. Three-dimensional monitoring of soil water content in a maize field using electrical resistivity tomography. Hydrol. Earth Syst. Sci. 17:595–609. doi:10.5194/hess-17-595-2013

Binley, A., S.S. Hubbard, J.A. Huisman, A. Revil, D.A. Robinson, K. Singha, and L.D. Slater. 2015. The emergence of hydrogeophysics for improved understanding of subsurface processes over multiple scales. Water Resour. Res. 51:3837–3866. doi:10.1002/2015WR017016

Binley, A., P. Winship, L.J. West, M. Pokar, and R. Middleton. 2002. Seasonal variation of moisture content in unsaturated sandstone inferred from borehole radar and resistivity profiles. J. Hydrol. 267:160–172. doi:10.1016/S0022-1694(02)00147-6

Bogena, H.R., C. Montzka, J.A. Huisman, A. Graf, M. Schmidt, M. Stockinger, et al. 2018. The TERENO-Rur Hydrological Observatory: A multiscale multi-compartment research platform for the advancement of hydrological science. Vadose Zone J. 17:180055. doi:10.2136/vzj2018.03.0055

Busch, S., J. van der Kruk, and H. Vereecken. 2014. Improved characterization of fine-texture soils using on-ground GPR full-waveform inversion. IEEE Trans. Geosci. Remote Sens. 52:3947–3958. doi:10.1109/TGRS.2013.2278297

Busch, S., L. Weihermüller, J.A. Huisman, C.M. Steelman, A.L. Endres, H. Vereecken, and J. van der Kruk. 2013. Coupled hydrogeophysical inversion of time-lapse surface GPR data to estimate hydraulic properties of a layered subsurface. Water Resour. Res. 49:8480–8494. doi:10.1002/2013WR013992

Cai, G., J. Vanderborght, A. Klotzsche, J. van der Kruk, J. Neumann, N. Hermes, and H. Vereecken. 2016. Construction of minirhizotron facilities for investigating root zone processes. Vadose Zone J. 15(9). doi:10.2136/vzj2016.05.0043

Dafflon, B., J. Irving, and W. Barrash. 2011. Inversion of multiple intersecting high-resolution crosshole GPR profiles for hydrological characterization at the Boise Hydrogeophysical Research Site. J. Appl. Geophys. 73:305–314. doi:10.1016/j.jappgeo.2011.02.001

Ferré, P.A., J.H. Knight, D.L. Rudolph, and R.G. Kachanoski. 1998. The sample areas of conventional and alternative time domain reflectometry probes. Water Resour. Res. 34:2971–2979. doi:10.1029/98WR02093

Galagedara, L.W., G.W. Parkin, J.D. Redman, and A.L. Endres. 2002. Temporal and spatial variation of soil water content measured by borehole GPR under irrigation and drainage. Proc. SPIE 4758:180–185. doi:10.1117/12.462253

Garré, S., I. Coteur, C. Wongleecharoen, T. Kongkaew, J. Diels, and J. Vanderborght. 2013. Noninvasive monitoring of soil water dynamics in mixed cropping systems: A case study in Ratchaburi Province, Thailand. Vadose Zone J. 12(2). doi:10.2136/vzj2012.0129

Garré, S., M. Javaux, J. Vanderborght, L. Pages, and H. Vereecken. 2011. Three-dimensional electrical resistivity tomography to monitor root zone water dynamics. Vadose Zone J. 10:412–424. doi:10.2136/vzj2010.0079

Huisman, J.A., S.S. Hubbard, J.D. Redman, and P.A. Annan. 2003. Measuring soil water content with ground penetrating radar: A review. Vadose Zone J. 2:476–491. doi:10.2136/vzj2003.4760

Huisman, J.A., J.J.J.C. Snepvangers, W. Bouten, and G.B.M. Heuvelink. 2002. Mapping spatial variation in surface soil water content: Comparison of ground-penetrating radar and time domain reflectometry. J. Hydrol. 269:194–207. doi:10.1016/S0022-1694(02)00239-1

Jaumann, S., and K. Roth. 2018. Soil hydraulic material properties and layered architecture from time-lapse GPR. Hydrol. Earth Syst. Sci. 22:2551–2573. doi:10.5194/hess-22-2551-2018

Jayawickreme, D.H., R.L. van Dam, and D.W. Hyndman. 2010. Hydrological consequences of land-cover change: Quantifying the influence of plants on soil moisture with time-lapse electrical resistivity. Geophysics 75:WA43–WA50. doi:10.1190/1.3464760

Klenk, P., S. Jaumann, and K. Roth. 2015. Quantitative high-resolution observations of soil water dynamics in a complicated architecture using time-lapse ground-penetrating radar. Hydrol. Earth Syst. Sci. 19:1125–1139. doi:10.5194/hess-19-1125-2015

Klotzsche, A., F. Jonard, M.C. Looms, J. van der Kruk, and J.A. Huisman. 2018. Measuring soil water content with ground penetrating radar: A decade of progress. Vadose Zone J. doi:10.2136/vzj2018.03.0052

Klotzsche, A., J. van der Kruk, G. He, and H. Vereecken. 2016. GPR full-waveform inversion of horizontal ZOP borehole data using gprMax. In: Proceedings of the 16th Conference on Ground Penetrating Radar, Hong Kong, China. 13–16 June 2016. IEEE, Piscataway, NJ. doi:10.1109/ICGPR.2016.7572695

Klotzsche, A., J. van der Kruk, N. Linde, J. Doetsch, and H. Vereecken. 2013. 3-D characterization of high-permeability zones in a gravel aquifer using 2-D crosshole GPR full-waveform inversion and waveguide detection. Geophys. J. Int. 195:932–944. doi:10.1093/gji/ggt275

Klotzsche, A., H. Vereecken, and J. van der Kruk. 2019. Review of crosshole GPR full-waveform inversion of experimental data: Recent developments, challenges and pitfalls. Geophysics 84:H13–H28. doi:10.1190/geo2018-0597.1

Linde, N., A. Binley, A. Tryggvason, L.B. Pedersen, and A. Revil. 2006. Improved hydro-geophysical characterization using joint inversion of cross-hole electrical resistance and ground-penetrating radar travel-time data. Water Resour. Res. 42:W12404. doi:10.1029/2006WR005131

Looms, M.C., A. Binley, K.H. Jensen, L. Nielsen, and T.M. Hansen. 2008a. Identifying unsaturated hydraulic parameters using an integrated data fusion approach on cross-borehole geophysical data. Vadose Zone J. 7:238–248. doi:10.2136/vzj2007.0087

Looms, M.C., K.H. Jensen, A. Binley, and L. Nielsen. 2008b. Monitoring unsaturated flow and transport using cross-borehole geophysical methods. Vadose Zone J. 7:227–237. doi:10.2136/vzj2006.0129

Michot, D., Y. Benderitter, A. Dorigny, B. Nicoullaud, D. King, and A. Tabbagh. 2003. Spatial and temporal monitoring of soil water content with an irrigated corn crop cover using surface electrical resistivity tomography. Water Resour. Res. 39(5):1138. doi:10.1029/2002WR001581

Parkin, G., D. Redman, P. von Bertoldi, and Z. Zhang. 2000. Measurement of soil water content below a wastewater trench using ground-penetrating radar. Water Resour. Res. 36:2147–2154. doi:10.1029/2000WR900129

Paz, C., F.J. Alcala, J.M. Carvalho, and L. Ribeiro. 2017. Current uses of ground penetrating radar in groundwater-dependent ecosystems research. Sci. Total Environ. 595:868–885. doi:10.1016/j.scitotenv.2017.03.210

Redman, D., G. Parkin, and P. Annan. 2000. Borehole GPR measurement of soil water content during an infiltration experiment. Proc. SPIE 4084:501–505. doi:10.1117/12.383619

Robinson, D.A., S.B. Jones, J.M. Blonquist, Jr., and S.B. Friedman. 2005. A physically derived water content/permittivity calibration model for coarse-textured, layered soils. Soil Sci. Soc. Am. J. 69:1372–1378. doi:10.2136/sssaj2004.0366

Rodríguez-Robles, U., T. Arredondo, E. Huber-Sannwald, J.A. Ramos-Leal, and E.A. Yepez. 2017. Technical note: Application of geophysical tools for tree root studies in forest ecosystems in complex soils. Biogeosciences 14:5343–5357. doi:10.5194/bg-14-5343-2017

Rossi, M., G. Manoli, D. Pasetto, R. Deiana, S. Ferraris, C. Strobbia, et al. 2015. Coupled inverse modeling of a controlled irrigation experiment using multiple hydro-geophysical data. Adv. Water Resour. 82:150–165. doi:10.1016/j.advwatres.2015.03.008

Roth, K., R. Schulin, H. Flühler, and W. Attinger. 1990. Calibration of time domain reflectometry for water content measurement using a composite dielectric approach. Water Resour. Res. 26:2267–2273.

Rudolph, S., J. van der Kruk, C. von Hebel, M. Ali, M. Herbst, C. Montzka, et al. 2015. Linking satellite derived LAI patterns with subsoil heterogeneity using large-scale ground-based electromagnetic induction measurements. Geoderma 241–242:262–271. doi:10.1016/j.geoderma.2014.11.015

Schmalholz, J., H. Stoffregen, A. Kemna, and U. Yaramanci. 2004. Imaging of water content distributions inside a lysimeter using GPR tomography. Vadose Zone J. 3:1106–1115. doi:10.2136/vzj2004.1106

Shanahan, P.W., A. Binley, W.R. Whalley, and C.W. Watts. 2015. The Use of electromagnetic induction to monitor changes in soil moisture profiles beneath different wheat genotypes. Soil Sci. Soc. Am. J. 79:459–466. doi:10.2136/sssaj2014.09.0360

Simmer, C., I. Thiele-Eich, M. Masbou, W. Amelung, H. Bogena, S. Crewell, et al. 2015. Monitoring and modeling the terrestrial system from pores to catchments. Bull. Am. Meteorol. Soc. 96:1765–1787. doi:10.1175/BAMS-D-13-00134.1

Steelman, C.M., and A.L. Endres. 2011. Comparison of petrophysical relationships for soil moisture estimation using GPR ground waves. Vadose Zone J. 10:270–285. doi:10.2136/vzj2010.0040

Steelman, C.M., D.R. Klazinga, A.G. Cahill, A.L. Endres, and B.L. Parker. 2017. Monitoring the evolution and migration of a methane gas plume in an unconfined sandy aquifer using time-lapse GPR and ERT. J. Contam. Hydrol. 205:12–24. doi:10.1016/j.jconhyd.2017.08.011

Strobach, E., B.D. Harris, J.C. Dupuis, and A.W. Kepic. 2014. Time-lapse borehole radar for monitoring rainfall infiltration through podosol horizons in a sandy vadose zone. Water Resour. Res. 50:2140–2163. doi:10.1002/2013WR014331

Topp, G.C., J.L. Davis, and A.P. Annan. 1980. Electromagnetic determination of soil water content: Measurements in coaxial transmission lines. Water Resour. Res. 16:574–582. doi:10.1029/WR016i003p00574

Vanella, D., G. Cassiani, L. Busato, J. Boaga, S. Barbagallo, A. Binley, and S. Consoli. 2018. Use of small scale electrical resistivity tomography to identify soil–root interactions during deficit irrigation. J. Hydrol. 556:310–324. doi:10.1016/j.jhydrol.2017.11.025

Vereecken, H., A. Schnepf, J.W. Hopmans, M. Javaux, D. Or, T. Roose, et al. 2016. Modeling soil processes: Review, key challenges, and new perspectives. Vadose Zone J. 15(5). doi:10.2136/vzj2015.09.0131

von Hebel, C., S. Rudolph, A. Mester, J.A. Huisman, P. Kumbhar, H. Vereecken, and J. van der Kruk. 2014. Three-dimensional imaging of subsurface structural patterns using quantitative large-scale multiconfiguration electromagnetic induction data. Water Resour. Res. 50:2732–2748. doi:10.1002/2013WR014864

Warren, C., A. Giannopoulos, and I. Giannakis. 2016. gprMax: Open source software to simulate electromagnetic wave propagation for ground penetrating radar. Comput. Phys. Commun. 209:163–170. doi:10.1016/j.cpc.2016.08.020

Weihermüller, L., J.S. Huisman, S. Lambot, M. Herbst, and H. Vereecken. 2007. Mapping the spatial variation of soil water content at the field scale with different ground penetrating radar techniques. J. Hydrol. 340:205–216. doi:10.1016/j.jhydrol.2007.04.013

Wijewardana, Y.G.N.S., and L.W. Galagedara. 2010. Estimation of spatio-temporal variability of soil water content in agricultural fields with ground penetrating radar. J. Hydrol. 391:24–33. doi:10.1016/j.jhydrol.2010.06.036

Wijewardana, Y.N.S., A.T. Shilpadi, M.I.M. Mowjood, K. Kawamoto, and L.W. Galagedara. 2017. Ground-penetrating radar (GPR) responses for sub-surface salt contamination and solid waste: Modeling and controlled lysimeter studies. Environ. Monit. Assess. 189:57. doi:10.1007/s10661-017-5770-4